



Full length article

Clarifying the irradiation effect on the general oxidation of 316L stainless steel in high temperature hydrogenated water after 1000h immersion

Shengkai Wang^a, Qi Wang^a, Shihao Zhang^a, Jiayu Xie^a, Miao Song^b, Wenjun Kuang^{a,*}^a Center for Advancing Materials Performance from the Nanoscale (CAMP-Nano), State Key Laboratory for Mechanical Behavior of Materials, Xi'an Jiaotong University, Xi'an 710049, China^b School of Nuclear Science and Engineering, Shanghai Jiao Tong University, Shanghai 200240, China

ARTICLE INFO

Keywords:

Stainless steel
General oxidation
Cr-enriched oxide
Ni-rich zone
Scanning transmission electron microscopy

ABSTRACT

The role of proton irradiation in the general oxidation of 316 L stainless steel in simulated PWR primary water after 1000 h immersion was clarified by comparing the microstructural and microchemical features of oxides formed on both the irradiated and un-irradiated regions of identical grains. Hence, the interference from differences in crystallographic orientation can be ruled out. Interestingly, the average inner oxide thickness on the irradiated region is significantly thinner than that on the un-irradiated region. The enhanced resistance to oxidation on the irradiated region originates from the more protective inner oxide layer and the formation of a continuous Ni-rich zone near the oxide/matrix interface. The inner oxide formed on irradiated region is less deficient in cation due to the enhanced diffusion of Cr from matrix by the irradiation-induced defects, thus making a better diffusion barrier. Meanwhile, the formation of continuous Ni-rich zone near the oxide/matrix interface, which is facilitated by the Ni-rich defects serving as nuclei, fast generation of vacancy at the interface and suppression of the outward diffusion of surplus Ni, can diminish the available space for the growth of inner oxide. The limited oxidation space and high Cr content at the oxide/matrix interface in the irradiated region result in the formation of rocksalt oxide while spinel oxide is formed near the interface in the un-irradiated region.

1. Introduction

The core internals of light water reactors are mainly fabricated from austenitic stainless steel as they exhibit good mechanical properties and high corrosion resistance. For Pressurized Water Reactors (PWRs), the major internal components are baffle/former plates made of solution annealed 304 stainless steel (SS) and baffle to former bolts made of cold worked 316 and/or 316 L SS. These components in PWR are subject to a corrosive environment, mechanical stress and neutron irradiation to a dose as high as ~80 dpa after 40 years of in-service life at temperatures between 300 and 370 °C [1–7]. Such harsh service conditions can lead to a degradation behavior known as Irradiation Assisted Stress Corrosion Cracking (IASCC) which can severely jeopardize the economy and safety of nuclear power plants. Oxidation is a basic form of corrosion for nuclear structure materials and is also a precursor of Stress Corrosion Cracking (SCC) as the crack initiation can be triggered when the oxide film is ruptured under stress [8]. Thus, it is crucial to determine the influence of irradiation on oxidation behavior in order to better

understand and predict Irradiation Assisted Corrosion (IAC) and IASCC.

The typical oxide film formed on austenitic stainless steels exposed to hydrogenated high temperature water has a dual-layer spinel structure (i.e., an outer layer of relatively large and scattered oxide particles and an inner continuous layer) [9–11]. The inner layer was reported to be protective and Cr-enriched while the outer layer is composed of Fe-rich magnetite [12–15]. Many researchers also found that a nickel-enriched layer was located at the inner oxide/matrix interface [15–17]. It is generally accepted that the formation of oxide film on alloy is controlled by the diffusion of oxygen vacancies and metal cations in materials [16, 18, 19]. Irradiation can influence the oxidation kinetics via inducing displacement damage in material and change the corrosive environment by water radiolysis [20–22]. In nuclear reactor conditions, the irradiation effect on oxidation due to accumulated displacement damage in material would be dominant as the radiolysis dose rate is normally low.

Currently, only a few studies have focused on the influence of irradiation-induced defects on the corrosion behavior of stainless steel. Due to the scarcity of neutron sources and relevant research facilities,

* Corresponding author.

E-mail address: wjkuang66@gmail.com (W. Kuang).<https://doi.org/10.1016/j.actamat.2023.119100>

Received 13 January 2023; Received in revised form 10 June 2023; Accepted 16 June 2023

Available online 17 June 2023

1359-6454/© 2023 Acta Materialia Inc. Published by Elsevier Ltd. All rights reserved.

ion irradiation has been normally used as an effective and economic surrogate for neutron irradiation at the lab research stage. Proton irradiation, when well controlled, can be used to mimic neutron irradiation and produce an irradiated layer deep enough for studying the general corrosion behavior [23]. There is still no clear conclusion on the effect of irradiation on general corrosion of stainless steel. Perrin et al. [1] studied the corrosion behavior of proton-irradiated 316 L stainless steel in simulated PWR primary water for 1024 h and found that the inner layer of irradiated sample is thinner than that of un-irradiated sample. In addition, they also found that the outer oxide particle formed on un-irradiated sample is larger than that on irradiated sample. The work from Dumerval [14] also suggested that in primary medium of PWR, smaller crystallites and thinner inner oxide were formed on Xe-irradiated 316 L stainless steel after 600 h of exposure to primary water. However, Deng et al. [24] reported that the inner oxide film formed on proton-irradiated 304 SS gets thicker with increasing irradiation dose after an immersion test in simulated PWR primary water for 500 h. Boisson et al. [25] reported a consistent trend: thicker inner oxides were formed on 1.5 dpa proton-irradiated 316 L austenitic stainless steel compared to the non-irradiated counterpart after exposure to simulated PWR primary water for 24 h. Jiao and Was [26] performed a constant extension rate tensile test on proton-irradiated 316 stainless steel (5 dpa) in simulated BWR environment for 70 h and pointed out that there is no significant difference in the average thickness of inner layer between the irradiated and un-irradiated parts of the sample. Thus, a consensus on the irradiation effect on the oxidation behavior of austenitic SS has not been achieved yet. These different and even opposite results may be caused by different experimental conditions (e.g., immersion time, irradiation dose et al.). Moreover, several studies on nickel-based alloys [27] and austenitic stainless steels [11,25,28] have shown that the crystallographic orientation of the metal substrate affects the oxidation kinetics. Hence, the dependence of oxidation resistance on grain orientation would obscure the irradiation effect on oxidation.

In this work, the general oxidation behavior of proton-irradiated 316 L stainless steel in high temperature hydrogenated water was investigated after 1000 h immersion test. Samples from the irradiated and non-

irradiated regions of the same grains were extracted for detailed analysis. As such, the influence of substrate orientation can be eliminated and the effect of irradiation on general oxidation can be clarified.

2. Experimental

2.1. Material and sample preparation

Solution-annealed (SA) 316 L austenitic stainless steel with chemical composition of 16.2 wt.% Cr, 10.11% Ni, 2.06% Mo, 1.58% Mn, 0.35% Si, 0.17% Co, 0.017% Ta, 0.001% S, 0.036% P, 0.37% Cu, 0.017% C and Fe balance was machined into square bars (10 mm × 2 mm × 2 mm) by electrical discharge machining (EDM). The sample was mechanically ground with silicon carbide papers to 2000 grit and then electropolished in alcohol solution consisting of 10% perchloric acid for 20 s at -40°C .

The proton irradiation experiment was performed at the Michigan Ion Beam Laboratory (MIBL) at University of Michigan with a 3 MeV Pelletron accelerator. The sample was irradiated with 2 MeV protons at $360 \pm 10^{\circ}\text{C}$ at a damage rate about 1×10^{-5} dpa/s to a dose of 2.5 dpa. The depth damage profile was estimated by SRIM 2013 [29] with quick Kinchin-Pease option using a displacement energy of 40 eV (shown in Fig. 1). Approximately half of the surface area of the sample was directly irradiated. The depth of proton damaged layer is around 20 μm and a nearly 15 μm thick uniformly-damaged region (UDR) was created. The irradiation induced defects were characterized and reported in our previous work [30].

2.2. Exposure test

Before the exposure test, the cross-section of proton-irradiated surface was polished. To avoid deformation and rounded corners near the edge of cross-section, another stainless steel square bar was mounted next to irradiated 316 L stainless steel bar during polishing. The cross-section of proton-irradiated surface was wet ground using silicon carbide papers up to 3000 grit, followed by mechanical polishing with 1.5 μm , 0.5 μm diamond polishing pastes successively, and finally vibration-polished with 60 nm colloidal silica polishing suspension for at least 3 h

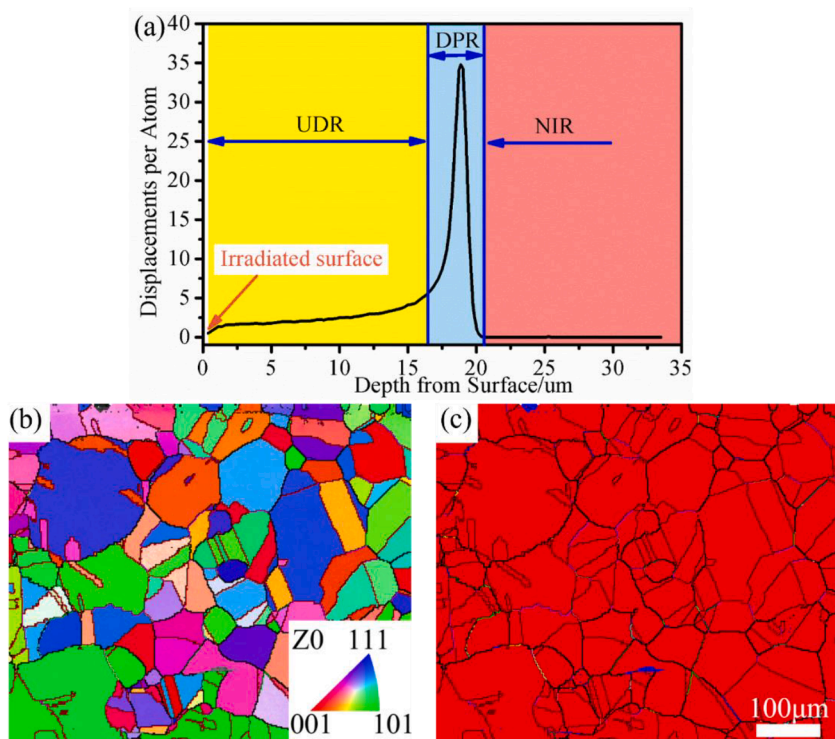


Fig. 1. (a) Damage profile for 316 L stainless steels irradiated with 2.0 MeV protons as calculated by SRIM 2013 computer code, (UDR represents uniformly-damaged region; DPR represents damage peak region; NIR represents non-irradiated region), (b) Inverse pole figure (IPF) overlaid with grain boundaries network from EBSD measurement (black-RHAB, red-twin boundary) on the cross-section of proton-irradiated surface, (c) phase map overlaid with grain boundaries (red-austenite, blue-ferrite).

to remove the deformed surface layer. To examine the grain orientation across the irradiated and non-irradiated regions, electron back scattering diffraction (EBSD) was conducted using an FEI Helios Nanolab 600 system equipped with a Nordlys EBSD detector. The EBSD images were obtained at a step size of $2\ \mu\text{m}$ with a voltage of 25 kV and a probe current of 5.5 nA. The exposure test was performed in the laboratory of Xi'an Jiao tong University. The sample was exposed to simulated PWR primary water ($320\ ^\circ\text{C}$, 150 bar, 30 cc $\text{H}_2/\text{kg}\ \text{H}_2\text{O}$) in a refreshed 3.6-L stainless steel autoclave at a flow rate of 12 L/h for 1000 h. During the test, the dissolved oxygen (DO) and conductivity of both inlet and outlet water were continuously monitored with Mettler Toledo sensors.

2.3. Analysis of general oxidation

After the exposure test, the samples were taken out from the autoclave for further characterization. According to a procedure used before [31], transmission electron microscopy (TEM) lamellae were cut using focused ion beam (FIB) milling in a FEI Helios Nanolab 600 and finally polished with 5 kV Ga^+ ion to a thickness of $\sim 90\ \text{nm}$. Fig. 2a shows the TEM lamellae extraction from UDR and NIR on the cross section of the irradiated surface. Both the UDR and non-irradiated regions (NIR) from nine grains with different crystallographic orientations were sampled. It should be noted that the TEM lamellae could be extracted from UDR and NIR precisely because: 1, there is a clear line corresponds to the damage peak region (DPR) on the EBSD band contrast map (as shown in Fig. 2) before exposure test; 2, a high density of oxide particles formed on DPR after exposure test. Moreover, analysis of the radiation defects in TEM lamellae confirms that the samples were extracted at the right regions. Fig. 2b and c show the TEM BF under-focus images of the matrix on UDR and NIR. Radiation defects (voids) were clearly observed on UDR (Fig. 2b) while not detected on NIR (Fig. 2c). High-angle annular

dark-field (HAADF) images were obtained using a JEOL JEM-F200(HR) microscope in scanning TEM (STEM) mode. With the aid of Image J software, the inner oxide layer was sectioned at an interval of $0.5\ \mu\text{m}$ across its length ($\sim 15\ \mu\text{m}$) and the average inner oxide thicknesses for each section were obtained by dividing the oxide area by the interval size. The overall average inner oxide thickness and standard deviation were calculated from the section averages. The values of error bar, which are the standard deviations of the measured thicknesses, reflect the homogeneity of the inner oxide layer. The chemical composition was analyzed in the JEOL JEM-F200(HR) which is equipped with two $100\ \text{mm}^2$ energy dispersive spectroscopy (EDS) detectors. Both EDS mapping (image resolution: 512×512 pixel, dwell time: 2 milliseconds) and line scanning (step size: $0.5 \sim 1\ \text{nm}$, probe size: 5) were conducted to reveal the microchemical features of the oxide. It should be noted that the counts of identified elements were used for EDS mapping. In addition, high-resolution STEM-HAADF images were taken in a FEI Tecnai G2 F30 microscope which is equipped with HAADF and EDS detectors. Fast Fourier Transformation (FFT) was used to analyze the high-resolution images.

2.4. Measurement of the inner oxide thickness from cross section

The oxide thickness was measured on TEM lamellae with STEM-HAADF to directly compare between UDR and NIR of the same grain matrix. In addition, SEM in back-scattered electron (BSE) mode was also used to measure the thickness on cross-section sample with large data volume. To confirm the difference in oxide thickness between irradiated and un-irradiated regions, the oxidized bar was cross sectioned and the general thickness of inner oxide was measured with statistical significance from both regions. The corrosion bar was Ni plated to avoid the shedding of oxide film during the grinding and polishing. The vibration-

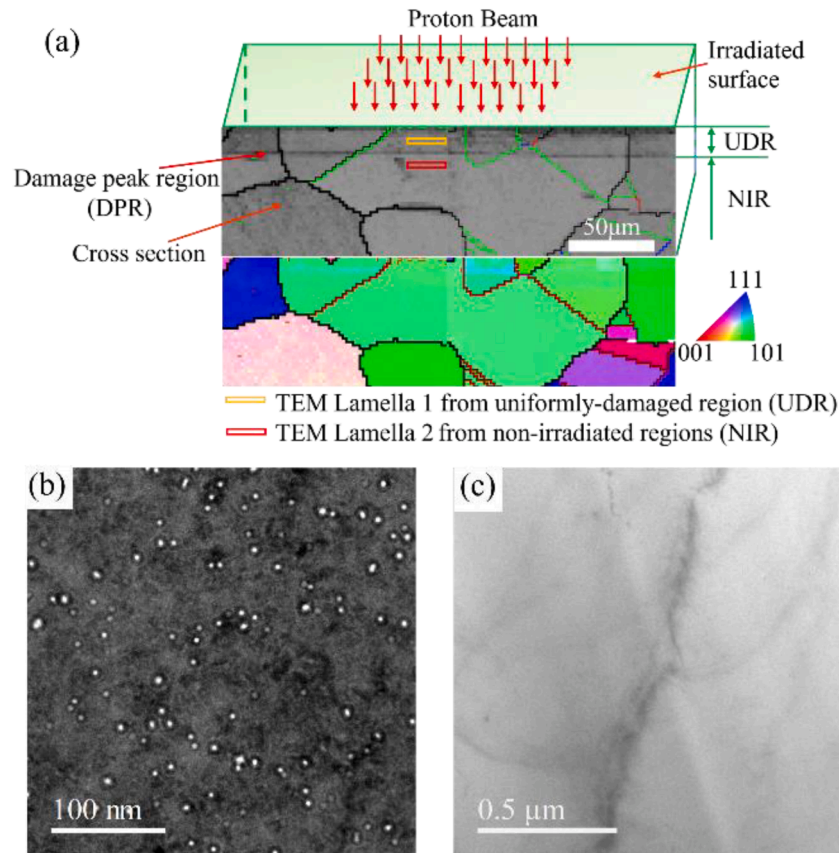


Fig. 2. (a) TEM lamellae extraction from UDR and NIR on the cross section of the irradiated surface, (b) TEM BF under-focus images of the matrix on UDR, (c) TEM BF under-focus images of the matrix on NIR.

polished cross-section was examined across both the irradiated and un-irradiated regions using a FEI Verios 460 SEM in BSE mode (beam voltage: 5 kV, probe current size: 0.4 nA). The damage peak region (DPR), which appears as a darker line under BSE mode, enables straightforward identification of the irradiated and un-irradiated regions. For each region, the inner oxide layer was sectioned at 1 μm intervals across a length of approximately 500 μm from BSE images. For each section, the average inner oxide thicknesses were obtained by dividing the oxide area by the interval size. The means and standard deviations of inner oxide thickness for both irradiated and un-irradiated regions were then calculated from those section averages.

3. Results

Fig. 1b and c show the inverse pole figure and phase map overlaid with grain boundary network from the EBSD measurement on the cross-section of proton-irradiated surface. The grains are mostly equiaxed and the average grain size is about 85 μm . There are a few ferrite stringers from the phase map (Fig. 1c). In this work, nine grains were sampled to evaluate the influence of irradiation on the general oxidation behavior. The crystallographic orientations of these nine grains were marked in the orientation triangle (shown in Fig. 3a). Fig. 3b summarizes the inner oxide thicknesses formed on UDR and NIR measured from eighteen lamellae (extracted from nine grains). Interestingly, the inner oxide

layer formed on the UDR is consistently thinner than that formed on NIR for all the sampled grains, regardless of the crystallographic orientation. The average inner oxide thickness from these grains is 98 ± 17 nm in UDR, much thinner than that in NIR (153 ± 30 nm). From Fig. 3b, the error bar in UDR is much smaller than that in NIR, indicating that the inner oxide layer in UDR is more homogenous than that in NIR. Fig. 3c-h shows the STEM-HAADF images of oxide scales formed on grains (Grain 7 (Fig. 3c and d), Grain 8 (Fig. 3e and f) and Grain 9 (Fig. 3g and h)) which are close to crystallographic orientations of (101), (111) and (100), respectively. The original sample surfaces were denoted by yellow dashed lines between the inner and outer oxides on STEM-HAADF images. As shown in Fig. 3c-h, the inner oxide layers on UDR are much thinner and more homogenous than those on NIR. Some voids were clearly observed in the matrix in UDR. The microchemical and microstructural characterizations of inner and outer oxides formed on nine grains were conducted and the results show very consistent features. Only the results from Grain 1 were presented here. The EDS results of oxide scales formed on another three grains (Grain 7, Grain 8 and Grain 9) were provided in the supplementary file.

After 1000 h oxidation, the surfaces of both UDR (Fig. 4a) and NIR (Fig. 4b) from Grain 1 are covered by dense outer oxide particles with different sizes. These faceted particles are mainly spinel [1,10,32–34], as confirmed in Fig. 8. The size distribution of oxide particles on UDR is more homogenous than that on NIR. Plus, the maximum diameter of

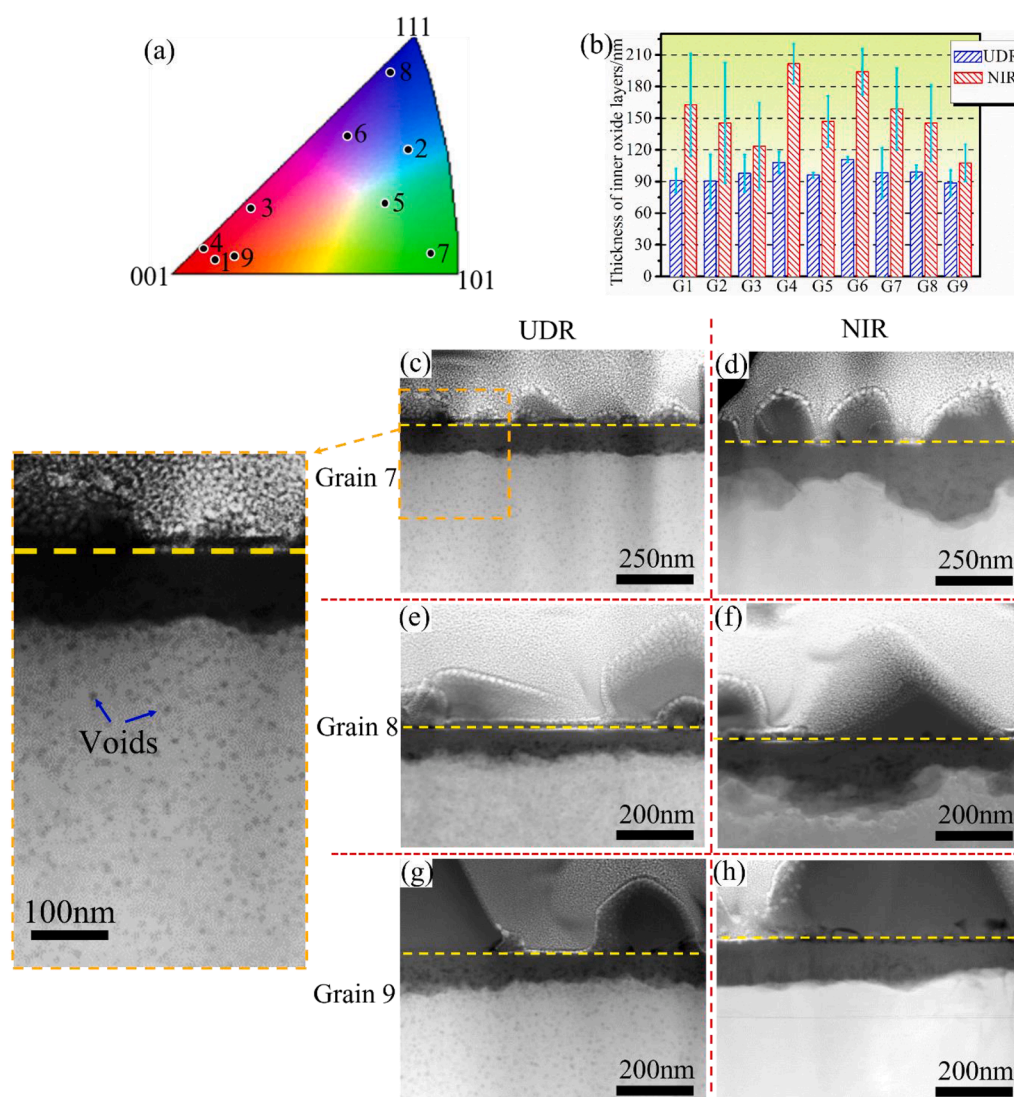


Fig. 3. (a) Crystal plane indices of the nine grains were marked in the orientation triangle, (b) Thicknesses of inner oxide formed on UDR and NIR of the nine grains (G represents Grain), STEM-HAADF images of oxide scales formed on (c) UDR and (d) NIR of Grain 7 which are close to the crystallographic orientation of [101], STEM-HAADF images of oxide scales formed on (e) UDR and (f) NIR of Grain 8 which are close to the crystallographic orientation of [111], STEM-HAADF images of oxide scales formed on (g) UDR and (h) NIR of Grain 9 which are close to the crystallographic orientation of [100].

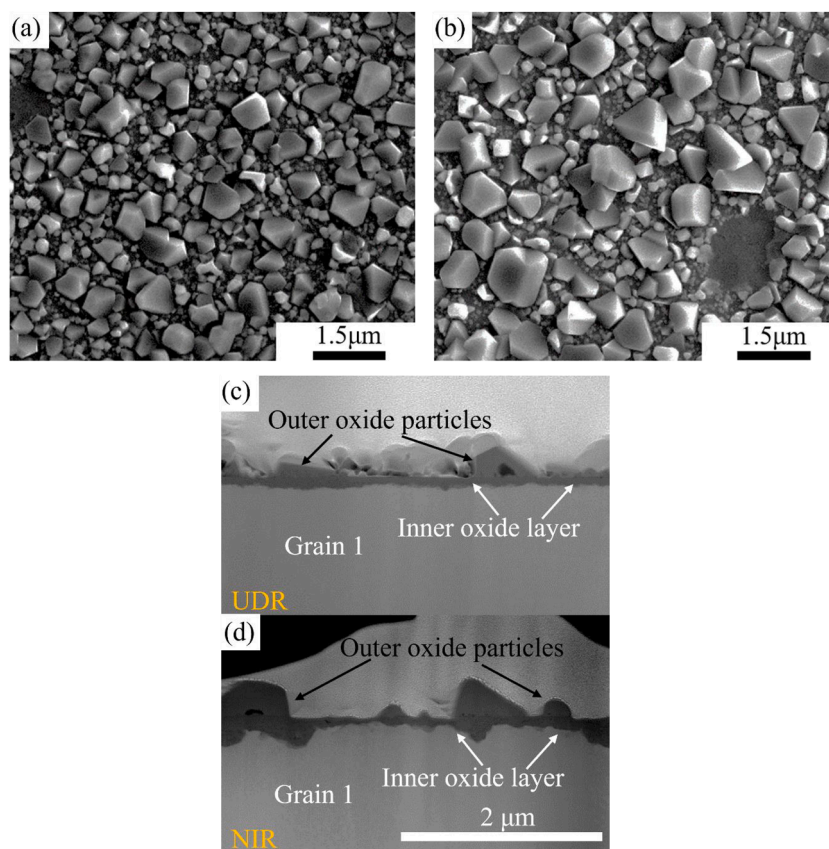


Fig. 4. SEM secondary electron (SE) images of outer oxide particles formed on (a) UDR and (b) NIR of Grain 1, STEM-HAADF images of the oxide scales formed on (c) UDR and (d) NIR.

outer oxide particle on UDR ($\sim 0.7 \mu\text{m}$) is much smaller than that on NIR ($\sim 1.3 \mu\text{m}$). In this work, the sample was exposed in a stainless steel autoclave and the problem of iron redeposition should be considered. The irradiated region and its un-irradiated counterpart are on the same grain and thus very close to each other (no more than $15 \mu\text{m}$). Thus, the effect of iron redeposition on oxidation kinetics should be similar between these two regions. Moreover, no correlation was observed between the morphology of outer oxide particles and the grain orientation. The orientation dependence of outer oxide morphology may be related to oxidation time. The redeposition of cations or maybe oxide particles in a stainless steel autoclave may cover up the original morphology of outer oxide particles after 1000 h immersion. Fig. 4c and d show the STEM-HAADF images of TEM lamellae extracted from UDR and NIR of Grain 1, respectively. A typical duplex oxide structure was observed on both UDR and NIR (Fig. 3c–h). The thickness of inner oxide layer on UDR of Grain 1 is $91 \pm 11 \text{ nm}$, much smaller than that on NIR ($163 \pm 49 \text{ nm}$). Moreover, the thickness of inner oxide layer on UDR is more homogeneous than that on NIR.

Fig. 5 shows the STEM-HAADF image (Fig. 5a), EDS mappings (Fig. 5b) and line scanning results (Fig. 5c) of oxide scale formed on UDR of Grain 1. From the EDS mappings shown in Fig. 5b, the outer oxide particle is enriched in Fe and Ni while depleted in Cr. The inner continuous oxide layer formed on matrix is Cr-enriched. A notable and continuous Ni-rich transition zone was detected at the matrix/inner oxide layer interface (Fig. 5b). Fig. 5c shows the EDS line profile across the oxide scale in Fig. 5a. A transition zone about 46 nm wide was detected near the inner oxide layer/matrix interface (Fig. 5c). From matrix to oxide, Fe content decreases rapidly (from $65.1 \text{ at.}\%$ to $16.7 \text{ at.}\%$) while Ni shows a peak and then declines below the matrix level. Compared with the composition in matrix (Ni: $9.3 \text{ at.}\%$, Cr: $17.3 \text{ at.}\%$), the maximum content of Ni in this transition zone is significantly

increased (up to $19.2 \text{ at.}\%$) and the average content of Cr is slightly decreased (down to $15.8 \text{ at.}\%$). The average contents of Cr and Ni in the inner oxide are $15.3 \text{ at.}\%$ and $4.6 \text{ at.}\%$, respectively. Fig. 6 shows the STEM-HAADF image (Fig. 6a), EDS mappings (Fig. 6b) and line scanning results (Fig. 6c) of oxide scale formed on NIR. As shown in Fig. 6b, the chemical distribution of outer oxide particle on NIR is similar to that on UDR, i.e., Fe and Ni are enriched while Cr is depleted. The inner oxide layer formed on matrix is also Cr-enriched as in UDR. Fig. 6c shows the EDS line profile across the oxide scale in Fig. 6a. From Fig. 6c, the width of transition zone is much smaller than that in Fig. 5c (14 nm vs. 46 nm). Moreover, the maximum content of Ni in the transition zone is significantly lower than that in Fig. 5c ($11.2 \text{ at.}\%$ vs. $19.2 \text{ at.}\%$). It should be noted that the transition zone beneath a relatively thinner oxide layer is always more enriched in Ni, as denoted in Fig. 6b. The content of Cr decreases across the transition zone and the average content is comparable to that in Fig. 5c ($15.6 \text{ at.}\%$ vs. $15.8 \text{ at.}\%$). The content of Fe decreases more abruptly across the transition zone in Fig. 6c. The average content of Cr in inner oxide (Fig. 6c) is lower than that in UDR (Fig. 5c) ($12.7 \text{ at.}\%$ vs. $15.3 \text{ at.}\%$). These results directly show the difference in microchemical composition of oxide between UDR and NIR which is caused by irradiation. The distribution of Ni in the inner oxide layer is heterogeneous. From the EDS line profile across the inner oxide layer, the average content of Ni in the lower part of inner oxide is significantly lower than that in the upper part ($2.5 \text{ at.}\%$ vs. $5 \text{ at.}\%$). The features of inner oxide layer and transition zone in UDR and NIR of all the sampled grains are summarized in Table 1. In summary, the average Cr content in inner oxide in UDR is higher than that in NIR. Meanwhile, the maximum Ni content in transition zone is higher and width of this zone is much larger in UDR. For Grain 1, the inner continuous oxide on UDR has a formulation of $(\text{Ni}_{0.28}\text{Fe}_{0.72})(\text{Fe}_{0.46}\text{Cr}_{0.54})_2\text{O}_4$ (Point A) while that in NIR has a formulation of $(\text{Ni}_{0.12}\text{Fe}_{0.88})(\text{Fe}_{0.63}\text{Cr}_{0.37})_2\text{O}_4$ (Point B) in the lower

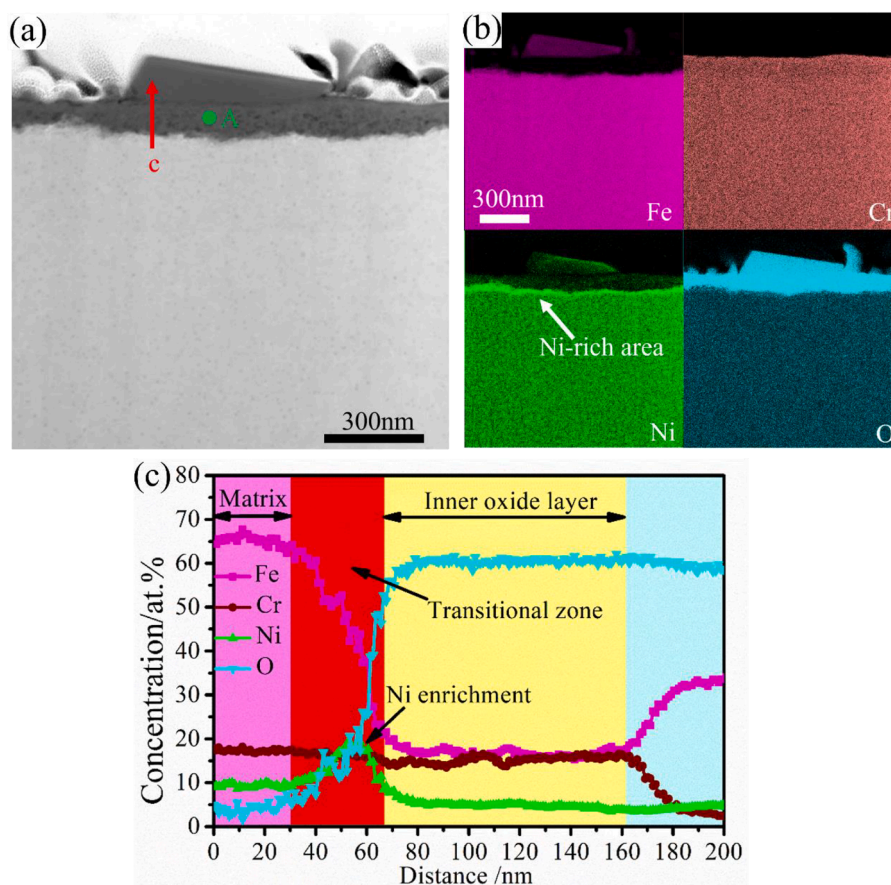


Fig. 5. (a) STEM-HAADF image, (b) EDS mappings and (c) EDS line scanning results of oxide scales formed on UDR of Grain 1.

part and $(\text{Ni}_{0.34}\text{Fe}_{0.66})(\text{Fe}_{0.63}\text{Cr}_{0.37})_2\text{O}_4$ (Point C) in the upper part (shown in Table 2). It should be noted that EDS is a semi-quantitative technique, but it is sensitive to cation concentration and accurate enough to reflect the significant difference in Ni content at the oxide/matrix interface. Fig. 7 shows the average contents of main elements in inner oxide measured from UDR and NIR of all the sampled grains by EDS line scanning. From Fig. 7, the average contents of Fe, Cr, Ni and O in inner oxide in UDR are 18.1 at.%, 17.2 at.%, 5.5 at.% and 56.29 at.%, respectively. While the corresponding percentages in NIR are 15.2 at.%, 14.9 at.%, 5.0 at.% and 61.5 at.%. The average contents of metallic elements in NIR are significantly lower than those in UDR. Fig. 7 gives a more direct comparison in the chemical composition of inner oxide layer between UDR and NIR. The difference in cation concentration is a vital evidence for revealing the irradiation effect.

Fig. 8a and b show the under-focus TEM-BF images of the oxide scales on UDR and NIR of Grain 1. Porosities were observed in both inner oxides (Fig. 8a and b). Fig. 8c and d show the SAED patterns taken from the corresponding circled areas in Fig. 8a and b. The diffraction patterns indicate that these inner oxides have a spinel-type structure which is epitaxial with the matrix, consistent with other finding [25]. The SAED patterns taken from the outer oxide particles in Fig. 8a and b also show a spinel structure (as shown in Fig. 8e and f). Combined with the EDS analyses presented above, it can be concluded that the inner oxide is Fe-Cr-Ni spinel and the outer oxide is Fe-Ni spinel. Thus, the crystal structures of inner oxide and outer oxide were basically not affected by proton irradiation.

The inner oxides formed on UDR and NIR were further analyzed through high resolution imaging. Fig. 9a shows the high-resolution STEM-HAADF images of inner oxide formed on UDR. The images were obtained with Grain 1 tilted to $\langle 110 \rangle$ zone axis. The inner oxide adjacent to matrix shows a rocksalt structure and the lattice spacing (0.239 nm) is

consistent with the (111) plane spacing of rocksalt MO oxide. Furthermore, a spinel structure was observed near the rocksalt structure with a (111) plane spacing of 0.479 nm. Fig. 9b shows the Fast Fourier Transformation (FFT) of the matrix and rocksalt structure. The rocksalt structure oxide has a cube-on-cube orientation relationship with the matrix. Fig. 10 shows the high-resolution STEM-HAADF images of inner oxide/matrix interface in NIR. Interestingly, the inner oxide shows a spinel structure and the lattice spacing (0.479 nm) is consistent with the (111) spacing of spinel (Fig. 10a). Fig. 10b and c show the FFTs of the matrix and inner oxide, respectively. The inner oxide has a spinel structure and maintains an epitaxial orientation relationship with matrix. Fig. 11 shows the high-resolution STEM-HAADF image and EDS mappings of the oxide/matrix interface in UDR and NIR. From Fig. 11a, a significant and continuous Ni-rich zone was observed just below the inner oxide layer. Moreover, Fe and Cr are depleted in this zone. There is no depletion of Ni beneath the Ni-rich zone, indicating that the Ni enrichment probably arises from the outward diffusion of Fe and Cr and back repulsion of Ni [17,35]. From Fig. 11b, a discrete Ni-rich zone was observed at the inner oxide/matrix interface in NIR. The enrichment of Ni is not as significant as in UDR. No obvious Cr depletion was detected in this zone. Interestingly, the inner oxide layer adjacent to the matrix has a rocksalt structure in UDR while it has a spinel structure in NIR. It should be noted that the rocksalt structure oxide adjacent to the matrix was also occasionally detected in NIR where the inner oxide layer is thinner.

The inner oxide thicknesses from the irradiated and un-irradiated regions were measured from the BSE images taken from the cross-section sample. Fig. 12a shows inner oxide layers from irradiated and un-irradiated regions. Consistent with the above results, the oxide layer formed on the irradiated region is much thinner and more homogeneous. Fig. 12b shows the distributions of measured inner oxide

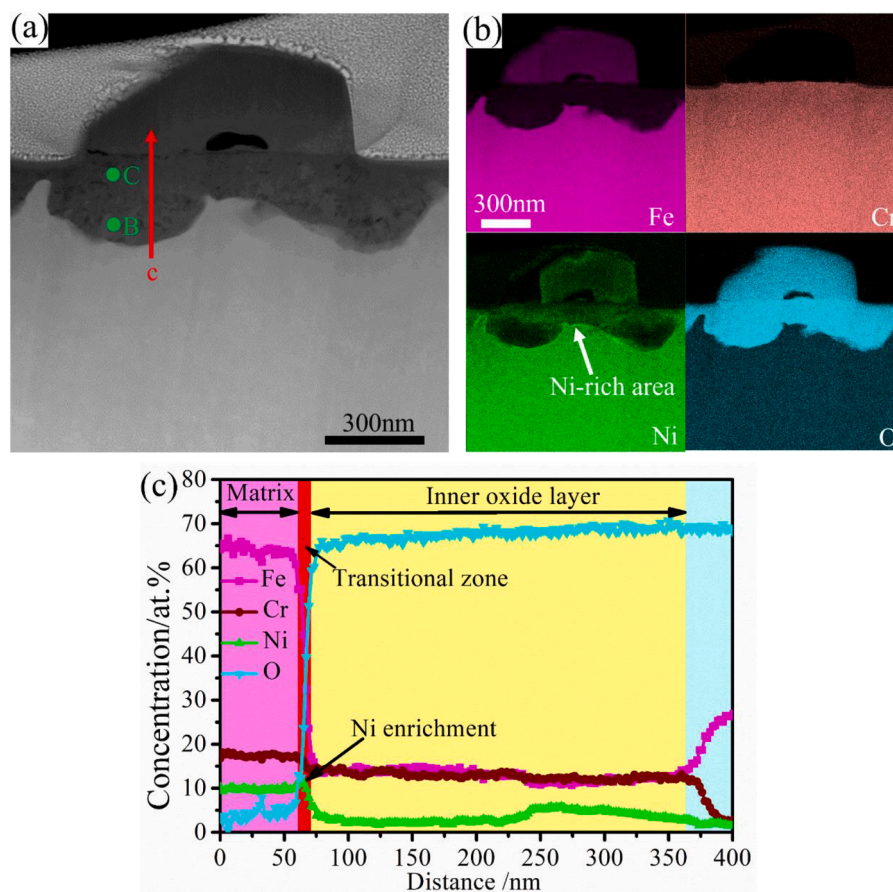


Fig. 6. (a) STEM-HAADF image, (b) EDS mappings and (c) EDS line scanning results of oxide scales formed on NIR of Grain 1.

Table 1

Average Cr content in inner oxide, maximum Ni content in Ni-rich zone, width of Ni-rich zone and average thickness of inner oxide layer of Grain X (X is 1 from 9).

Grain		Ave. Cr content in inner oxide (at.%)	Max. Ni content in transitional zone (at.%)	Width of Ni-rich zone (nm)	Ave. inner oxide thickness (nm)
Grain 1	UDR	15.7	19.2	46	91 ± 11
1	NIR	12.8	11.2	14	163 ± 49
Grain 2	UDR	16.3	20.5	72	90 ± 25
2	NIR	13.1	12.1	25	145 ± 57
Grain 3	UDR	16.5	19.5	47	98 ± 18
3	NIR	15.8	9.7	5	123 ± 42
Grain 4	UDR	18.0	19.6	73	108 ± 10
4	NIR	16.4	11.8	18	202 ± 19
Grain 5	UDR	18.6	20.2	50	96 ± 8
5	NIR	16.2	11.6	18	147 ± 24
Grain 6	UDR	16.3	18.5	58	111 ± 13
6	NIR	15.3	11.5	24	194 ± 22
Grain 7	UDR	17.2	19.6	67	98 ± 24
7	NIR	15.9	11.7	20	159 ± 39
Grain 8	UDR	18.4	19.0	52	99 ± 7
8	NIR	15.8	11.1	15	146 ± 36
Grain 9	UDR	16.5	22.6	70	89 ± 12
9	NIR	14.0	11.3	16	108 ± 18

thicknesses. The average thicknesses of inner oxide formed on irradiated and un-irradiated regions are 118 ± 21 nm and 193 ± 33 nm, respectively. The difference in average inner oxide thickness between UDR and NIR is 65%, which is quite consistent with that obtained from the previously sampled grains, confirming that the resistance to general oxidation after 1000 h immersion can be enhanced by irradiation.

Table 2

Results of the EDS point analysis of the oxide scale (shown in Figs. 5 and 6) and the calculated stoichiometry of the spinel oxide formed on UDR and NIR.

Point	O (at. %)	Cr (at. %)	Fe (at. %)	Ni (at. %)	Spinel stoichiometry
Point A (UDR)	60.66	16.55	15.88	4.21	$(\text{Ni}_{0.28}\text{Fe}_{0.72})(\text{Fe}_{0.46}\text{Cr}_{0.54})_2\text{O}_4$
Point B (NIR)	67.85	12.59	13.97	2.10	$(\text{Ni}_{0.12}\text{Fe}_{0.88})(\text{Fe}_{0.63}\text{Cr}_{0.37})_2\text{O}_4$
Point C (NIR)	67.48	12.39	11.51	5.81	$(\text{Ni}_{0.34}\text{Fe}_{0.66})(\text{Fe}_{0.63}\text{Cr}_{0.37})_2\text{O}_4$

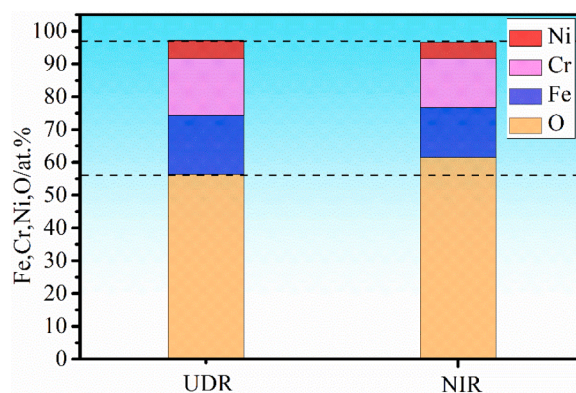


Fig. 7. Average contents of Fe, Cr, Ni and O in inner oxide formed on UDR and NIR.

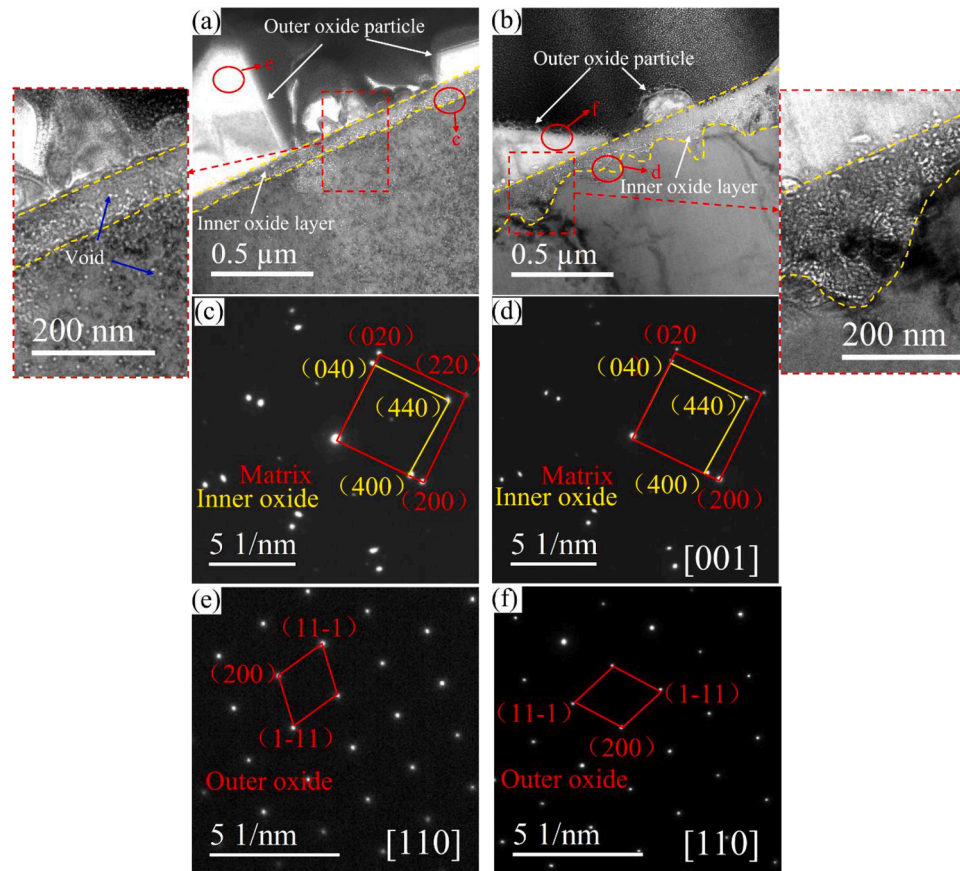


Fig. 8. TEM BF under-focus images of the oxide scales and matrix on (a) UDR and (b) NIR, SAED patterns of inner oxide layer combined with matrix on (c) UDR and (d) NIR, SAED patterns of outer oxide particles on (e) UDR and (f) NIR.

4. Discussion

The above results show that proton irradiation inhibits the general oxidation of 316 L stainless steel after 1000 h immersion regardless of the crystallographic orientation of matrix. The microstructural and microchemical features of oxides formed on both UDR and NIR will be analyzed. Afterwards, the effect of irradiation on general oxidation behavior will be discussed based on the results.

4.1. Irradiation effect on the general oxidation of stainless steel

The proton irradiation induced defects in stainless steel mainly consist of Frank loops and voids. The average number density and diameter of Frank loops have been reported in our previous work [30] and the results are consistent with those reported in proton and neutron irradiated austenitic stainless steels [23,36–38]. The average number density and size of these voids in TEM lamella from UDR are $5.9 \pm 3.6 \times 10^{21} \text{ m}^{-3}$ and $6.0 \pm 1.4 \text{ nm}$, respectively.

The average inner oxide thickness on NIR is much larger than that on UDR ($193 \pm 33 \text{ nm}$ vs. $118 \pm 21 \text{ nm}$) and the direct comparison between NIR and UDR of the same grains also confirms this trend (Fig. 3). Moreover, the morphology of outer oxide particles is similar between UDR and NIR of the same grain while significant difference exists in the size distribution. The outer oxide particles on UDR are more homogeneous and have smaller diameters than those on NIR (Fig. 4a and b). Thus, irradiation induced damage also influences the formation of outer oxide particles. Overall, proton irradiation has a significant mitigation effect on the growth of inner and outer oxides after 1000 h immersion.

The inhibition effect of proton irradiation on general oxidation observed in this work is inconsistent with some of the previous works

[24,25]. There are two main factors causing such inconsistency. First of all, the interference from the dependence of oxidation on grain orientation was not accounted for in the previous works. It has been reported that the generation oxidation rate of 316 L stainless steel in simulated PWR primary water is dependent on the crystallographic orientation of grain matrix [11,28]. The variation in the thickness of inner oxide layer among different grains (Fig. 3) also confirms such dependence. A false conclusion would be drawn if one compared the oxide thickness from UDR of Grain 6 with that from NIR of Grain 9 (Fig. 3b). Thus, it is imperative to eliminate the interference caused by different grain orientations in order to single out the effect of irradiation on oxidation rate. The inhibition effect of irradiation on the general oxidation of stainless steel can be confirmed in this work as we not only compared oxide thickness between the two regions within the same grains (Fig. 3), but also sampled large areas to get results with statistical significance (Fig. 12). Another factor that needs to be considered is the duration of exposure test. It should be noted that the immersion time is up to 1000 h in this work. Boisson et al. [25] found that the inner oxide layer on irradiated region is more than 5 times thicker than that on the non-irradiated region after short immersion duration (24 h). The results of Deng et al. [24] are also contrary to ours. They proposed that irradiation defects could accelerate the diffusion of oxygen and cation and result in a thicker inner oxide after 500 h immersion. These inconsistencies might result from the difference in oxidation time because the displacement damage induced by irradiation probably exhibits different effects on oxidation kinetics at different stages. Indeed, the findings from Perrin et al. [1] are consistent with the results in this work. They conducted immersion test in simulated PWR primary water for 1024 h and found that the oxygen diffusion is slower in the Cr-rich inner oxide layer formed on the irradiated sample which was attributed to the

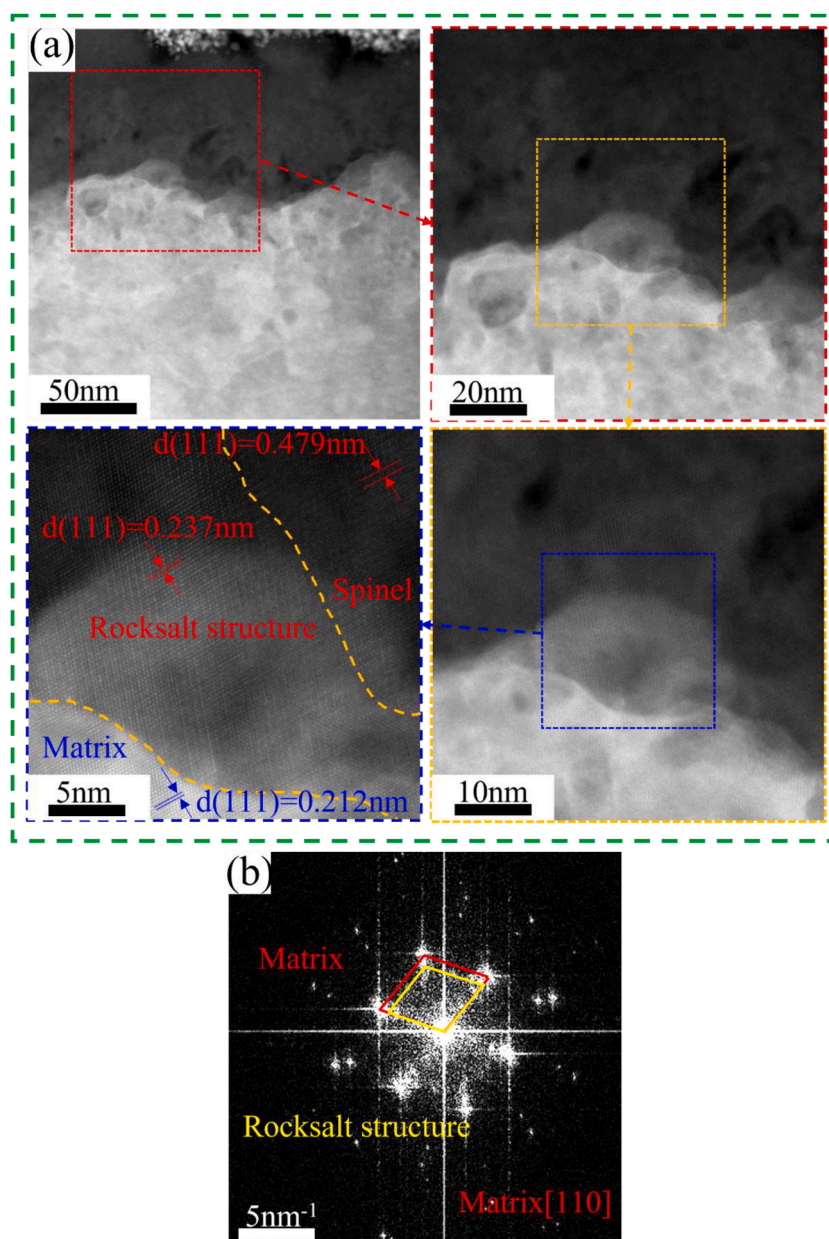


Fig. 9. (a) High resolution STEM-HAADF images of inner oxide and matrix from UDR, (b) Fast Fourier Transformation (FFT) of the matrix and adjacent inner oxide.

accelerated diffusion of Cr by irradiation induced defects. The time dependence of irradiation effect on the general oxidation of stainless steel will be further studied in our future work.

The difference in oxidation kinetics should be linked to the different microstructural and microchemical features of the oxide layer. An inner continuous oxide layer formed on both UDR and NIR after 1000 h immersion test (Fig. 4c and d), as has been reported in previous studies [24, 25]. The STEM-HAADF images, EDS mappings and line scans shown in Figs. 5 and 6 reveal differences in the microchemistry of inner oxide layer between UDR and NIR. The inner oxide formed on UDR is more enriched in Cr than that on NIR, as listed in Table 1. More importantly, the total cation fraction of inner oxide on UDR is much higher when compared with that on NIR (Fig. 7). A notable and continuous Ni-rich layer was observed near the inner oxide/matrix interface in UDR while only discrete Ni-rich zones were detected in NIR (shown in Figs. 5 and 6). The Ni-rich layer is just beneath the inner oxide layer and the Ni content is about 20 at.% which is much higher than the matrix level (Fig. 5). The inner oxide lattice adjacent to the Ni-rich zone shows

rocksalt structure in UDR, while spinel structure was observed near the inner oxide/matrix interface in NIR (shown in Figs. 9, 10 and 11). Thus, the higher cation content (especially Cr) in the inner oxide layer and the presence of continuous Ni-rich layer beneath the inner oxide are probably linked to the slower oxidation rate of UDR.

4.2. The origin of enhanced oxidation resistance for irradiated region

The inner continuous Cr-rich spinel oxide layer is the main barrier layer for oxidation [39] which prevents the metal from directly contacting the high temperature water. Further oxidation occurs by the outward diffusion of metal cations from matrix and the inward diffusion of oxygen from high temperature water through the inner oxide layer. Hence, the property of inner oxide layer is crucial to the oxidation resistance of stainless steel. The average Cr content in inner oxide on UDR is higher than that on NIR (shown in Table 1). Terachi et al. [16] reported that a slight difference in Cr content of inner oxide can result in significantly different oxidation resistance in simulated PWR primary

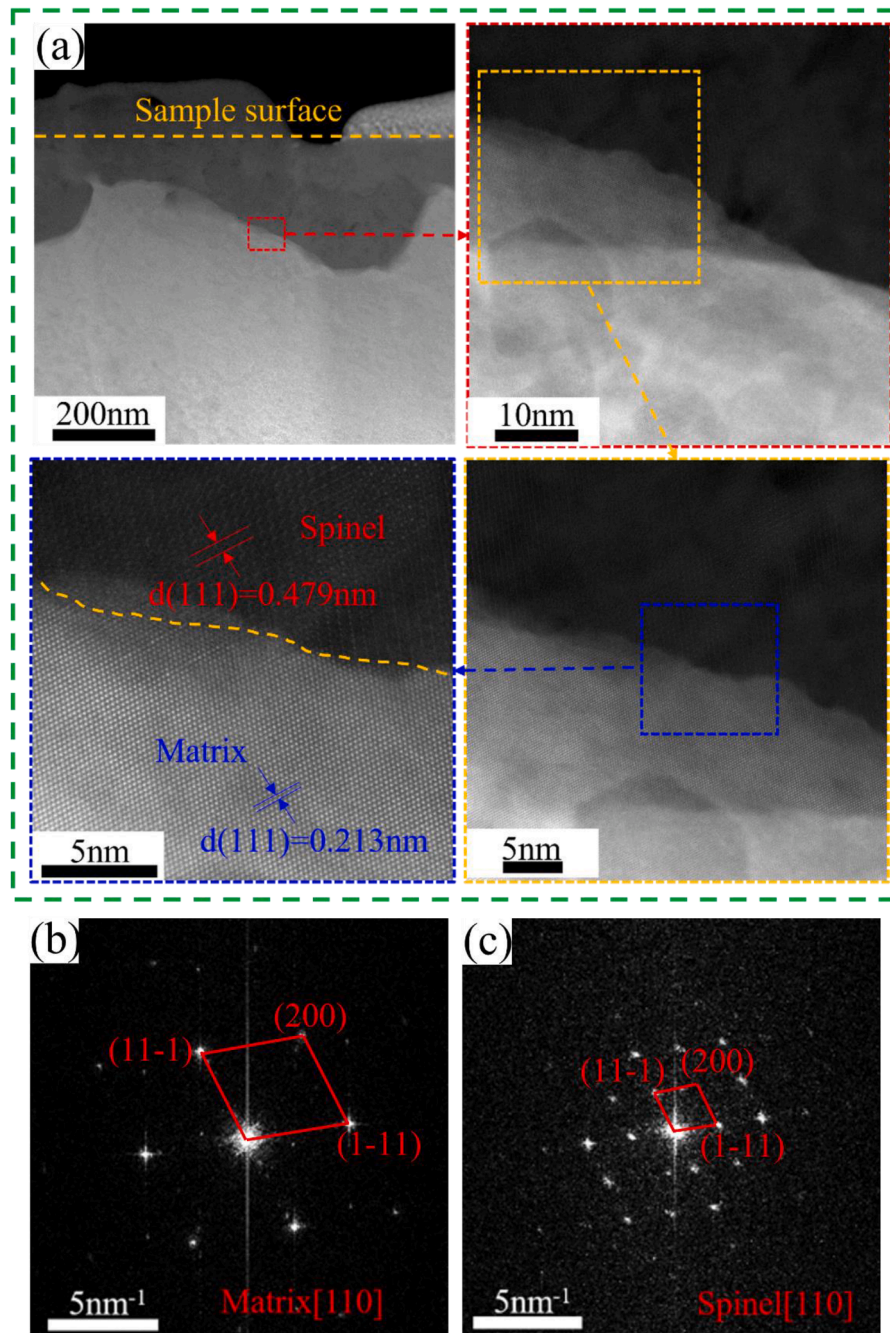


Fig. 10. (a) High resolution STEM-HAADF images of inner oxide and matrix from NIR, (b) Fast Fourier Transformation (FFT) of the matrix, (c) Fast Fourier Transformation (FFT) of the inner oxide.

water for stainless steel. According to their research, when the Cr content in inner oxide increases from 12.7 at.% to 15.3 at.%, the diffusion rate of Fe through inner oxide decreases by 25.9%. Thus, the elevated Cr content in inner oxide in UDR can enhance the resistance to general oxidation and eventually lead to a lower oxidation rate for the irradiated region after 1000 h immersion.

In addition to the difference in Cr content of inner oxide, some other factors may also play a role in the oxidation resistance. Some previous works [17,40–42] proposed that the Ni-rich zone near the inner oxide/matrix interface could act as a diffusion barrier for oxygen and suppress further oxidation. Kanzaki et al. [43] studied the effect of Ni content on the oxide thickness on alloys with a wide range of Ni content (10 mass.% to 70 mass.%) in 360 °C simulated PWR primary water and found that the oxide thickness decreased with increasing Ni content.

Fig. 11a clearly shows that the oxygen signal weakens abruptly when reaching the Ni-rich layer. It seems the mitigation effect of increased Ni on general oxidation in simulated PWR primary water is ubiquitous, but the underlying mechanism is not clear. It should be noted that the dual layer structure of oxide scale formed on stainless steel in high temperature water bears lots of resemblances to those formed on low alloy steel in liquid Pb-Bi and high temperature CO₂ [44–46]. An “available space model” has been proposed to explain the formation process of such a dual-layered oxide scale [45,46]. According to this model, the outer oxide is formed via the outward diffusion of cation through the nano-channels within the inner oxide layer; the inner oxide develops at the oxide/matrix interface via the oxidation of chemically-altered matrix and consumes the nano-cavities left by cation diffusion. More importantly, the rate determining step of inner oxide growth is the

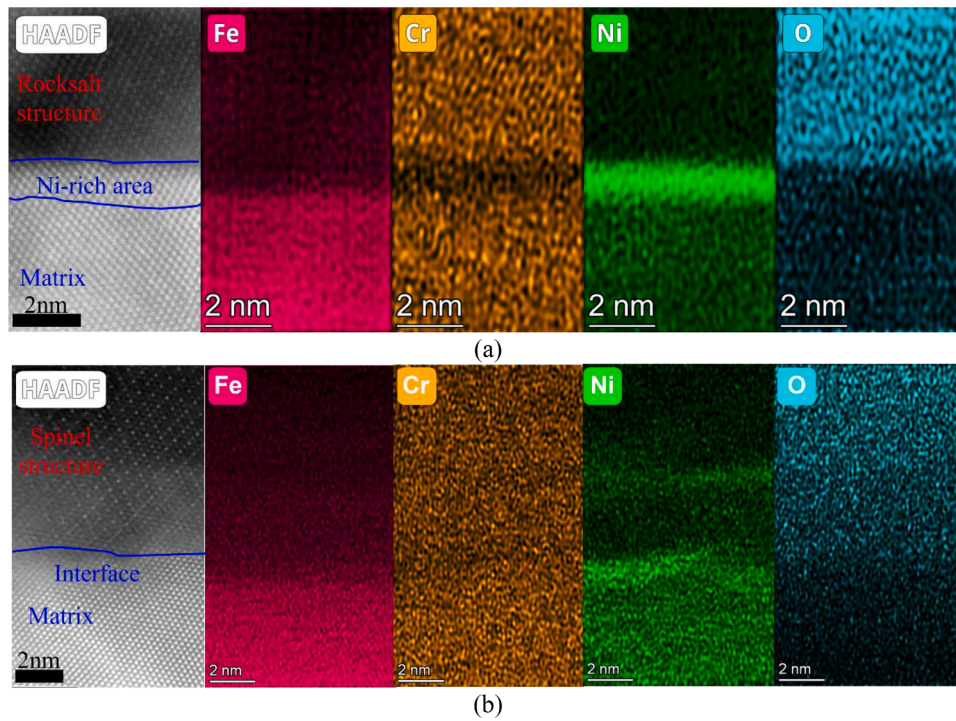


Fig. 11. High resolution STEM-HAADF images and EDS mappings of the inner oxide/matrix interface in (a) UDR and (b) NIR.

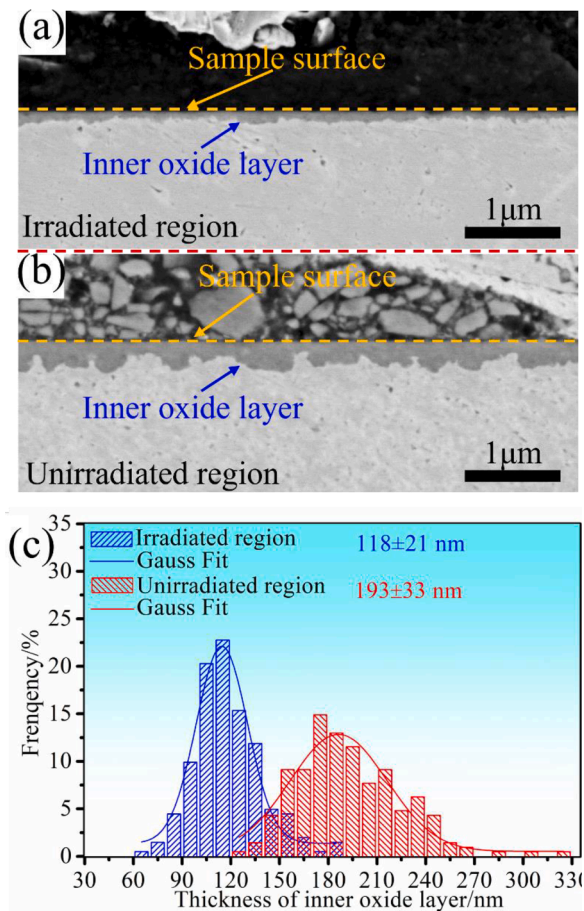


Fig. 12. . BSE images of cross-sectioned specimen showing the inner oxide layer from (a) irradiated and (b) unirradiated regions, (c) Bar charts of measured inner oxide thicknesses from the irradiated and unirradiated regions.

formation of nano-cavities at the interface which is dictated by the diffusion of cation across the inner oxide layer. Compared to the oxidations in liquid Pb-Bi and high temperature CO₂, the major difference in oxidation in high temperature water is that the cations would dissolve into high temperature water and some of them precipitate on the sample surface as oxide particles [10,33]. Nevertheless, such model should still apply to the formation of inner oxide layer in high temperature water. From the “available space model”, the transportation ability of inner oxide layer is a key factor which determines the oxidation rate. Fig. 7 shows that the inner oxide formed on NIR is more deficient in cation than that on UDR, suggesting that the oxide layer on NIR probably contains more vacancy-channels. Therefore, the oxide layer on NIR serves as a more efficient diffusion path and supports a higher oxidation rate. In contrast, the oxide layer on UDR is a better diffusion barrier and the outward diffusion of surplus cation (especially Ni) is suppressed to some extent. In this case, the redundant Ni would back fill some of the nano-vacancies, thus diminishing the “available space” for the growth of inner oxide layer. That explains why there is a continuous Ni-rich layer beneath the thinner oxide layer formed on UDR (Fig. 5) and why the Ni-rich zone enhances resistance to oxidation.

As mentioned above, the inner oxide lattice adjacent to the matrix in UDR shows rocksalt structure while that in NIR has a spinel structure. The formation of oxide with NiO-structure and mixed cations has also been reported in Ni base alloy (referred to as MO oxide) [47–50]. The formation of a rocksalt MO oxide in preference to spinel should be due to the limited available space and the high Cr content at the interface. Oxidation leads to volume expansion and gives rise to energy penalty to the system when the space is limited. As mentioned above, the redundant Ni consumes some of the nano-cavities and diminishes the space for oxidation. The formation of rocksalt MO oxide would induce less strain energy as its Pilling-Bedworth ratio (less than 2) is much smaller than that of spinel (above 2.2). Table 3 lists the Gibbs formation energy of related oxides at 600 K [52]. The data for MO is not available while NiO and FeO are used instead, but the trend should be similar. The Gibbs formation energy decreases in the order of NiO, FeO and spinel. Although the reduction in Gibbs free energy for the formation of spinel oxide is larger than that of rocksalt MO oxide, the energy penalty due to

Table 3

The Gibbs formation energy of the related oxides at 600 K [52].

Oxide	Structure	ΔG_f (kJ/mol)
NiO	Rocksalt	-183.967
FeO	Rocksalt	-231.691
NiFe ₂ O ₄	Spinel	-865.223
FeCr ₂ O ₄	Spinel	-1253.730
NiCr ₂ O ₄	Spinel	-1163.071

volume expansion is much smaller in the formation of rocksalt oxide. In addition, it has been reported that the incorporation of Cr into rocksalt oxide can greatly reduce its Gibbs energy [51]. Overall, the generation of rocksalt MO oxides requires a lower equilibrium oxygen partial pressure than the formation of spinel oxides (as confirmed by the calculation provided in Appendix A), implying that the formation of rocksalt MO oxides is more favorable. It should be noted that the “available oxidation space” at the oxide/matrix interface in NIR is relatively sufficient as the surplus cations can diffuse outwards through the defective inner oxide layer. Thus, the strain energy due to the volume expansion during oxidation can be neglected. In this case, the equilibrium oxygen partial pressure for forming spinel oxide is lower and the formation of spinel oxide is more favorable (shown in Appendix A).

In summary, the higher protectiveness of inner oxide and a continuous Ni-rich layer near the inner oxide/matrix interface in UDR are responsible for the enhanced resistance to general oxidation after 1000 h immersion. A continuous Ni-rich layer in UDR corresponds to a more homogenous inner oxide layer and sporadic Ni-rich areas in NIR are linked to a disturbed oxide/matrix interface (shown in Figs. 5 and 6).

4.3. The mechanism of irradiation effect on the general oxidation of stainless steel

The enhanced oxidation resistance of UDR should be eventually linked to the irradiation-induced defects. Irradiation induced defects (e.g., dislocation loops, voids et al.) can promote the lattice diffusion of metal atoms toward the oxidation front [1,53,54]. It is worth noting that the damage defects (e.g., deformation bands, dislocations and sub-grain boundaries et al.) induced by surface deformation can also facilitate the diffusion of Cr to the metal/oxide interface from the matrix in high temperature water, resulting in a protective inner oxide layer with increased Cr content [55–57]. In this study, a significant Cr-depleted zone was detected near the inner oxide/matrix interface (Fig. 11a). The Cr-depleted and Ni-enriched zones almost overlap each other. The formation of such zone should result from the short-range preferential diffusion of Cr to the oxidation front. Since the inner oxide layer on UDR has higher Cr content than that on NIR (Table 1), it is inferred that the irradiation-induced defects in UDR enhance the outward diffusion of Cr and increase the protectiveness of formed inner oxide layer. Hence, the outward diffusion of cations across the inner oxide layer is slower in UDR than in NIR, leading to a higher content of cations in inner oxide in UDR (Fig. 7). In contrast, faster cation diffusion across the inner oxide layer on NIR results in the formation of outer oxide particles with larger diameter and a thicker inner oxide layer. The larger variation in the size of oxide particles on NIR corresponds to the more heterogeneous inner oxide layer thickness (Fig. 4).

As for the formation of continuous Ni-rich layer near the inner oxide/matrix interface, given that there is no Ni depletion beneath the Ni-rich layer (Fig. 11), such Ni enrichment can't be induced by Ni diffusion from the matrix. The probable process is the outward diffusion of other metal elements (Cr and Fe) from this zone and the expulsion of surplus Ni from the inner oxide layer, as have been suggested in previous works [17,25]. A continuous Ni-rich layer tends to form in UDR due to the following possible reasons. First of all, Ni segregates at the irradiation-induced defects like dislocation loops, voids and some solute clusters [25,

58–60]. Such high-density defects can serve as nuclei for the formation of such continuous Ni-rich layer. In contrast, only sporadic Ni-rich areas form in NIR probably due to the lack of suitable nuclei. In addition, as the outward diffusion of Cr to oxidation front is promoted in UDR, the enhanced flux of Cr to oxide layer would cause more Ni to back fill the vacancies left behind by Cr atoms. Furthermore, as mentioned above, the inner oxide of UDR is more protective and can hinder the outward diffusion of Ni more effectively [61,62]. Therefore, the surplus Ni atoms created at the oxidation front in UDR tend to accumulate at the inner oxide/matrix interface while those in NIR are inclined to diffuse to the upper part of inner oxide (shown in Fig. 6) and finally enter into the solution.

Porosity of oxide layer was also believed to affect its protectiveness. Generally, the pores in the oxide layer result from the loss of cations (mostly Fe and Ni) to the environment [63] and the inheritance of irradiation-induced voids during the post-irradiation oxidation experiment [30]. The pores in oxide can act as fast path for oxygen transportation [63]. However, it should be pointed out that the pores can effectively promote the diffusion only when they are connected, as proposed in the work of Shen et al. [35]. In this work, it is difficult to differentiate the porosity of inner oxide between UDR and NIR (Fig. 8a and b). It's probably because the number density of voids at a dose of 2.5 dpa is not high enough to form a continuous pore network. Thus, the scattered voids induced by irradiation should have limited effect on the general oxidation rate. In contrast, our results (not shown here) indicate that for the DPR which corresponds to a dose of 35 dpa (Fig. 1), a higher density of voids result in continuous pore networks and eventually lead to a much higher general oxidation rate on DPR than those on UDR and NIR.

The processes of general corrosion for UDR and NIR of an identical grain after 1000 h immersion are summarized in Fig. 13. The inner oxide formed on UDR (Fig. 13a) is less defective than that formed on NIR due to the enhanced diffusion of active elements (especially Cr) by the irradiation-induced defects. The less defective oxide layer on UDR can

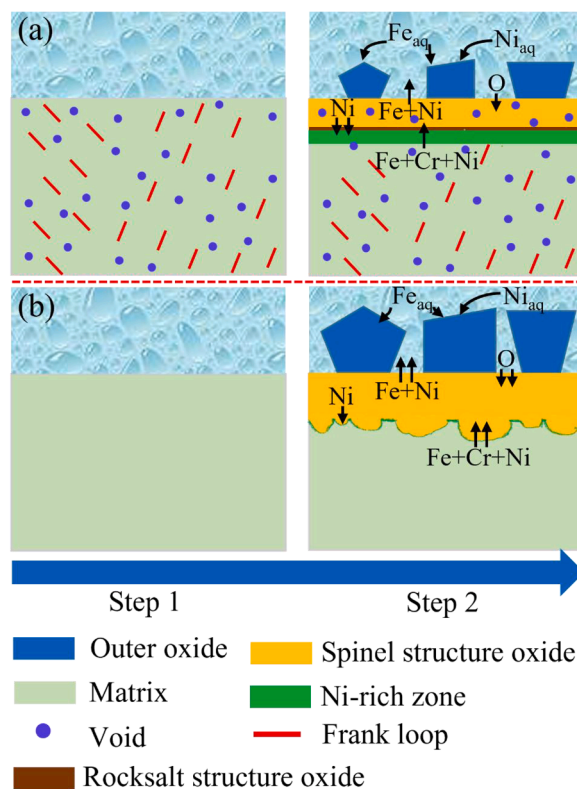


Fig. 13. Schematic of general corrosion for the (a) irradiated region and (b) unirradiated region of an identical grain.

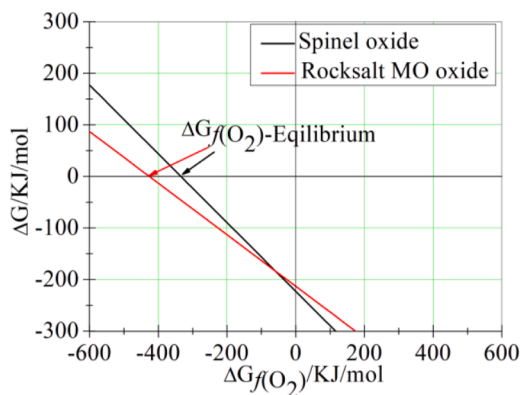


Fig. A1. The change in energy of the system due to oxidation (ΔG_{MO} and $\Delta G_{M_3O_4}$) at 600 K as a function of the Gibbs free energy of O_2 ($\Delta G_{f(O_2)}$).

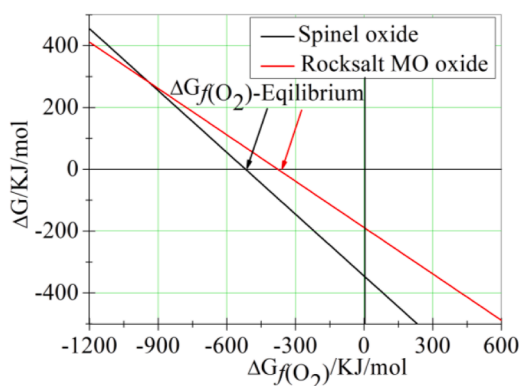


Fig. A2. The change in Gibbs free energy of the oxidation reaction ($\Delta G_{f(MO)}$ and $\Delta G_{f(M_3O_4)}$) at 600 K as a function of the Gibbs free energy of O_2 ($\Delta G_{f(O_2)}$).

server as a better diffusion barrier and hence reduce the oxidation rate. In addition, a notable continuous Ni-rich layer forms at the matrix/inner oxide layer interface in UDR (Fig. 13a). There was no obvious Ni-rich zone near the inner oxide/matrix interface in NIR (Fig. 13b). The inner oxide lattice adjacent to the Ni-rich zone shows rocksalt structure in UDR, while spinel structure was observed near most of the oxide/matrix interface in NIR. The Ni-rich zone near the inner oxide/matrix interface in UDR can further suppress the oxidation reaction by diminishing the available space for oxide growth. In summary, the combination of less defective inner oxide layer and a continuous Ni-rich layer near the inner oxide/matrix interface results in decelerated oxidation in irradiated region. This study clarifies the effect of post proton irradiation on general oxidation of austenitic stainless steel after 1000 h immersion in simulated PWR primary water by ruling out the influence of crystallographic orientation. Contradictory to conventional wisdom, the irradiation induced damages in the substrate material exhibit an inhibitory effect on the general oxidation rate. This work can shed light on the effect of in-situ irradiation on the oxidation of internal components in PWR. Given that the radiolysis dose rate in real reactor is very low, the primary difference between post irradiation and in-situ irradiation tests is that the oxide film itself is under irradiation in the latter case. From the work of Raiman and Was [21], it seems that irradiation induces

significant porosity in the preformed oxide layer on 316 L stainless steel. Investigation into the effect of irradiation damage in oxide layer on the subsequent oxidation will further improve our understanding of the oxidation behavior in realistic reactor conditions. It is also of great significance to study the effects of irradiation on grain boundary oxidation although this paper is intended to focus on general oxidation. Some results on intergranular oxidation have been reported in our previous work [54] and further results will be presented in the near future.

5. Conclusion

This work clarified the effects of proton irradiation on general corrosion behavior of 316 L stainless steel after exposure to simulated PWR primary water for 1000 h by ruling out the interference from the difference in crystallographic orientation. The conclusions are summarized as follows:

- 1 The inner oxide layer formed on the non-irradiated region (NIR) is thicker and more heterogeneous than that on the uniformly-damaged region (UDR) regardless of the crystallographic orientation, suggesting that proton irradiation has a mitigation effect on general oxidation after 1000 h immersion. The oxide layer on UDR has a notable continuous Ni-rich layer near the oxide/matrix interface and rocksalt oxide forms adjacent to the Ni-rich layer.
- 2 The enhanced oxidation resistance on UDR is related to the higher protectiveness of inner oxide layer and the continuous Ni-rich zone formed near the oxide/matrix interface. The inner oxide layer formed on UDR is a better diffusion barrier as it is less defective. In addition, the formation of continuous Ni-rich zone diminishes the “available space” for oxidation.
- 3 The irradiation-induced defects in UDR have profound effects on the oxide structure. They can enhance the outward diffusion of Cr and increase the protectiveness of formed inner oxide layer. Meanwhile, the formation of continuous Ni-rich layer near the inner oxide/matrix interface is facilitated by the Ni-rich defects serving as nuclei, available space generated at the interface due to promoted diffusion and suppression of the outward diffusion of surplus Ni.

Declaration of Competing Interest

The authors declare that they have no known competing financial interests or personal relationships that could have appeared to influence the work reported in this paper.

Acknowledgements

The authors gratefully acknowledge the financial support of National Natural Science Foundation of China (52271068 and 51971172) and the Young Talent Support Plan of Xi'an Jiaotong University. The authors thank Dr. Jiao Li at Instrument Analysis Center of Xi'an Jiaotong University for her assistance with STEM and EDS analysis, and research fellow Wei Wang for his assistance in SEM characterization. The authors also thank Prof. Gary S. Was from the University of Michigan for his assistance in the preparation of this work. The authors are grateful to Ziguang Chen from Huazhong University of Science & Technology and Kang Wang from University of Virginia for their help in discussion on the results.

Supplementary materials

Supplementary material associated with this article can be found, in the online version, at [doi:10.1016/j.actamat.2023.119100](https://doi.org/10.1016/j.actamat.2023.119100).

Appendix A. Detailed procedure for calculating the change in system energy induced by oxidation (ΔG_{MO} and $\Delta G_{M_3O_4}$)

Fig. A1, Fig. A2.

Although spinel oxide is generally more thermodynamically favorable than rocksalt MO oxide, the rocksalt indeed forms underneath inner spinel oxide in UDR in this work. There are several reasons behind this phenomenon: 1, As has been discussed in our manuscript, the stability of rocksalt oxide can be promoted by the addition of other cations, such as Cr. Sherman et al., [52] have reported that the incorporation of Cr into the rocksalt structure could reduce its free energy. The rocksalt oxide here indeed contains a significant amount of Cr (Fig. 11). 2, The change in energy of the system (ΔG) caused by the formation of oxides should include both Gibbs free energy and the strain energy due to the volume expansion during oxidation. Comparing the ΔG values of forming rocksalt structure oxide and spinel oxide can determine which oxide is preferentially formed. ΔG can be expressed as:

$$\Delta G = \Delta G_r + \Delta G_v \quad (1)$$

where ΔG is the change in energy of the system, ΔG_r is the change in Gibbs free energy, ΔG_v is the energy penalty for the volume expansion induced by oxidation.

$$\Delta G_v = P \cdot \Delta V \quad (2)$$

Where P is the stress induced by volume expansion, ΔV is the change in volume due to the oxidation of 1 mol metal. Here, P is not available and the yield strength (σ_y) of oxide is used instead.

$$\Delta V = V_O - V_M \quad (3)$$

Where V_O is the volume of oxide generated by 1 mole of metal, V_M is the volume of 1 mole metal.

For spinel structure oxide: $M + \frac{2}{3}O_2 = \frac{1}{3}M_3O_4$

$$\Delta G_r = \frac{1}{3}\Delta G_{f(M_3O_4)} - \frac{2}{3}\Delta G_{f(O_2)} - \Delta G_{f(M)} \quad (4)$$

Where $\Delta G_{f(M_3O_4)} = -1094 \text{ kJ/mol}$, $\Delta G_{f(M)} = -19.3 \text{ kJ/mol}$. Here the temperature is set to 600 K. Those data are obtained from Ref. [51]. It should be noted that $\Delta G_{f(M_3O_4)}$ is the average value of $\Delta G_{f(NiFe_3O_4)}$, $\Delta G_{f(NiCr_3O_4)}$ and $\Delta G_{f(FeCr_3O_4)}$, and $\Delta G_{f(M)}$ is the average value of $\Delta G_{f(Fe)}$, $\Delta G_{f(Ni)}$ and $\Delta G_{f(Cr)}$. Thus, ΔG_r and $\Delta G_{f(O_2)}$ have a linear relationship:

$$\Delta G_r = \frac{2}{3}\Delta G_{f(O_2)} + \frac{1}{3}\Delta G_{f(M_3O_4)} - \Delta G_{f(M)} = -\frac{2}{3}\Delta G_{f(O_2)} - 345.4 \quad (5)$$

The average Pilling-Bedworth ratio (PBR) of spinel oxide ($NiFe_2O_4$, $FeCr_2O_4$, $NiCr_2O_4$) is 2.24 (e.g., $\frac{V_O}{V_M} = 2.24$). The PBR calculation is described in Ref. [64]. The average molar volume (V_{mol}) of spinel oxide ($NiFe_2O_4$, $FeCr_2O_4$ and $NiCr_2O_4$) is $43.65 \text{ cm}^3/\text{mol}$. Thus,

$$\Delta V = V_O - V_M = V_O - \frac{V_O}{2.24} = 0.55V_O \quad (6)$$

Where V_O is $14.55 \text{ cm}^3 (\frac{1}{3}V_{mol})$. Thus, ΔV is 8.0 cm^3 .

The yield strength (σ_y) of spinel oxide is estimated to be 15.3 GPa at 600 K based on Ref. [65]. According to Ref. [65], the Young's modulus and the yield strength of the oxide can be described as $E_{ox} = E_{ox}^0(1 + n(T - 25))$ and $\sigma_y \approx \frac{E_{ox}}{10}$, respectively. Where E_{ox}^0 is the Young's modulus at 25 °C, T is the oxidation temperature and n is a constant. From Ref. [65], E_{ox}^0 and constant n are 210 GPa and -4.7×10^{-4} , respectively. Thus, yield strength is 15.3 GPa at 600 K. It should be noted that the yield strength (σ_y) of Fe_3O_4 is used instead as the data on other spinel oxides is not available. Thus, $\Delta G_v = P \cdot \Delta V = 122.6 \text{ kJ/mol}$,

$$\Delta G_{M_3O_4} = \Delta G_r + \Delta G_v = -\frac{2}{3}\Delta G_{f(O_2)} - 345.4 + 122.6 = -\frac{2}{3}\Delta G_{f(O_2)} - 222.8 \quad (7)$$

For rocksalt MO oxide: $M + \frac{1}{2}O_2 = MO$

$$\Delta G_r = \Delta G_{f(MO)} - \frac{1}{2}\Delta G_{f(O_2)} - \Delta G_{f(M)} \quad (8)$$

Where $\Delta G_{f(MO)} = -207.8 \text{ kJ/mol}$, $\Delta G_{f(M)} = -19.3 \text{ kJ/mol}$ at 600 K (from Ref. [51]). It should be noted that $\Delta G_{f(MO)}$ is the average value of $\Delta G_{f(NiO)}$ and $\Delta G_{f(FeO)}$ and $\Delta G_{f(M)}$ is the average value of $\Delta G_{f(Fe)}$, $\Delta G_{f(Ni)}$ and $\Delta G_{f(Cr)}$. Thus, ΔG_r is linearly related to $\Delta G_{f(O_2)}$:

$$\Delta G_r = -\frac{1}{2}\Delta G_{f(O_2)} + \Delta G_{f(MO)} - \Delta G_{f(M)} = -\frac{1}{2}\Delta G_{f(O_2)} - 188.5 \quad (9)$$

It should be noted that the incorporation of Cr into the rocksalt MO oxide further reduces the Gibbs formation energy ($\Delta G_{f(MO)}$) [52]. Therefore, Eq. (9) needs to be modified. According to Ref. [52], the Gibbs formation energy of rocksalt MO oxide ($\Delta G_{f(MO)}$) and Cr content (f) roughly show a linear

relationship at 1000 K as follows: $\Delta G_{f(MO)} = -275f-180$. Unfortunately, the data at 600 K is not available and can only be estimated. Assuming such linear relationship with the same slope rate is maintained at 600 K, the Gibbs formation energy of rocksalt MO oxide ($\Delta G_{f(MO)}$) with a Cr fraction of f can be described as: $\Delta G_{f(MO)} = -275f-207.8$. The Cr content in rocksalt MO oxide in this work is about 26.4 at.% ($[Cr]/([Fe]+[Cr]+[Ni])$). Thus, the Gibbs formation energy of rocksalt MO oxide ($\Delta G_{f(MO)}$) at 600 K is -280.4 kJ/mol . Then Eq. (9) can be modified as:

$$\Delta G_r = -\frac{1}{2}\Delta G_{f(O_2)} + \Delta G_{f(MO)} - \Delta G_{f(M)} = -\frac{1}{2}\Delta G_{f(O_2)} - 261.1 \quad (10)$$

The average Pilling-Bedworth ratio of rocksalt MO oxide (NiO , FeO) is 1.8 (e.g., $\frac{V_O}{V_M} = 1.8$). The average molar volume (V_{mol}) of rocksalt oxide is $11.67 \text{ cm}^3/\text{mol}$.

$$\Delta V = V_O - V_M = V_O - \frac{V_O}{1.8} = 0.44V_O \quad (11)$$

Where V_O is 11.67 cm^3 . Thus, ΔV is 5.1 cm^3 .

The yield strength (σ_y) of rocksalt MO oxide is 9.5 GPa at 600K which is also obtained from Ref. [65]. According to Ref. [65], E_{ox}^0 and constant n are 130 GPa and -4.7×10^{-4} , respectively. Thus, yield strength is 9.5 GPa at 600K. It should be noted that the yield strength (σ_y) of FeO is used instead as the data on rocksalt MO oxide is not available. Thus, $\Delta G_V = P \cdot \Delta V = 48.0 \text{ kJ/mol}$,

$$\Delta G_{MO} = \Delta G_r + \Delta G_V = -\frac{1}{2}\Delta G_{f(O_2)} - 213.1 \quad (12)$$

Fig. A1 is the change in energy of the system due to oxidation (ΔG_{MO} and $\Delta G_{M_3O_4}$) at 600 K as a function of the Gibbs free energy of O_2 ($\Delta G_{f(O_2)}$). As shown in Fig. A1, $\Delta G_{f(O_2)}$ in equilibrium with rocksalt MO oxide is smaller than that with spinel oxide, suggesting the oxygen partial pressure for forming MO oxide is lower and the formation of rocksalt oxide is more favorable in this case. Therefore, beneath a protective oxide film, although the Gibbs free energy of spinel oxide is lower than that of rocksalt oxide, the formation of rocksalt oxide is more favorable because the energy penalty due to volume expansion is much smaller and incorporation of Cr further reduces the Gibbs free energy.

It should be noted that the “available oxidation space” at the oxide/matrix interface in NIR is relatively sufficient as there is no continuous Ni-rich layer formed that can consume the “available space” for the growth of inner oxide layer. Thus, the strain energy due to the volume expansion during oxidation can be neglected in this case and only the change in Gibbs free energy of the reaction needs to be considered. Fig. A2 is the change in Gibbs free energy of the oxidation reaction ($\Delta G_{r(MO)}$ and $\Delta G_{r(M_3O_4)}$) at 600 K as a function of the Gibbs free energy of O_2 ($\Delta G_{f(O_2)}$). As shown in Fig. A2, $\Delta G_{f(O_2)}$ in equilibrium with spinel oxide is smaller than that with rocksalt MO oxide, suggesting the oxygen partial pressure for forming spinel oxide is lower and the formation of spinel oxide is more favorable in this case.

References

- [1] S. Perrin, L. Marchetti, C. Duhamel, M. Sennour, F. Jomard, Influence of irradiation on the oxide film formed on 316L stainless steel in PWR Primary Water, *Oxid. Met.* 80 (2013) 623–633.
- [2] B. Pastina, J.A. LaVerne, Effect of molecular hydrogen on hydrogen peroxide in water radiolysis, *J. Phys. Chem. A* 105 (2001) 9316–9322.
- [3] J. Gupta, Intergranular Stress Corrosion Cracking of Ion Irradiated 304L SS in PWR Environment, INP Toulouse, 2016. PhD thesis.
- [4] G.S. Was, K.J. Stephenson, Crack initiation behavior of neutron irradiated model and commercial stainless steels in high temperature water, *J. Nucl. Mater.* 444 (2014) 331–334.
- [5] M.D. Mcmurtrey, G.S. Was, Role of slip behavior in the irradiation assisted stress corrosion cracking in austenitic steels, in: *Proceedings of the 15th International Conference on Environmental Degradation of Materials in Nuclear Power Systems-Water Reactors*, Colorado, USA, Colorado Springs, 2011.
- [6] K. Fukuya, M. Nakano, K. Fujii, T. Torimaru, IASCC susceptibility and slow tensile properties of highly-irradiated 316 stainless steels, *J. Nucl. Sci. Technol.* 41 (2004) 673–681.
- [7] W. Kuang, G.S. Was, A high-resolution characterization of the initiation of stress corrosion crack in Alloy 690 in simulated pressurized water reactor primary water, *Corros. Sci.* 163 (2020), 108243.
- [8] Y.S. Lim, S.S. Hwang, D.J. Kim, M.J. Choi, S.H. Cho, The effect of surface oxidation on the IASCC susceptibility of proton-irradiated type 316 stainless steel in hydrogenated PWR primary water, in: *Proceedings of the Transactions of the Korean Nuclear Society Virtual Autumn Meeting*, 2021.
- [9] M. da Cunha Belo, M. Walls, N.E. Hakiki, J. Corset, E. Picquenard, G. Sagon, D. Noël, Composition, structure and properties of the oxide films formed on the stainless steel 316L in a primary type PWR environment, *Corros. Sci.* 40 (1998) 447–463.
- [10] B. Stellwag, The mechanism of oxide film formation on austenitic stainless steels in high temperature water, *Corros. Sci.* 40 (1998) 337–370.
- [11] R. Soulas, M. Cheynet, E. Rauch, T. Neisius, L. Legras, C. Domain, Y. Brechet, TEM investigations of the oxide layers formed on a 316L alloy in simulated PWR environment, *J. Mater. Sci.* 48 (2013) 2861–2871.
- [12] R.L. Tapping, R.D. Davidson, E. McAlpine, D.H. Lister, The composition and morphology of oxide films formed on type 304 stainless steel in lithiated high temperature water, *Corros. Sci.* 26 (1986) 563–576.
- [13] S. Cissé, L. Laffont, B. Tanguy, M.C. Lafont, E. Andrieu, Effect of surface preparation on the corrosion of austenitic stainless steel 304L in high temperature steam and simulated PWR primary water, *Corros. Sci.* 56 (2012) 209–216.
- [14] M. Dumerval, S. Perrin, L. Marchetti, M. Sennour, F. Jomard, S. Vaubailon, Y. Wouters, Effect of implantation defects on the corrosion of 316L stainless steels in primary medium of pressurized water reactors, *Corros. Sci.* 107 (2016) 1–8.
- [15] T. Terachi, K. Fujii, K. Arioka, Microstructural characterization of SCC crack tip and oxide film for SUS 316 stainless steel in simulated PWR primary water at 320°C, *J. Nucl. Sci. Technol.* 42 (2005) 225–232.
- [16] T. Terachi, T. Yamada, T. Miyamoto, K. Arioka, K. Fukuya, Corrosion behavior of stainless steels in simulated PWR primary water—Effect of chromium content in alloys and dissolved hydrogen, *J. Nucl. Sci. Technol.* 45 (2008) 975–984.
- [17] K. Kruska, S. Lozano-Perez, D.W. Saxey, T. Terachi, T. Yamada, G.D.W. Smith, Nanoscale characterisation of grain boundary oxidation in cold-worked stainless steels, *Corros. Sci.* 63 (2012) 225–233.
- [18] D.H. Lister, R.D. Davidson, E. McAlpine, The mechanism and kinetics of corrosion product release from stainless steel in lithiated high temperature water, *Corros. Sci.* 27 (1987) 113–140.
- [19] D.D. Macdonald, The history of the Point Defect Model for the passive state: a brief review of film growth aspects, *Electrochim. Acta* 56 (2011) 1761–1772.
- [20] S.S. Raiman, D.M. Bartels, G.S. Was, Radiolysis driven changes to oxide stability during irradiation-corrosion of 316L stainless steel in high temperature water, *J. Nucl. Mater.* 493 (2017) 40–52.
- [21] S.S. Raiman, G.S. Was, Accelerated corrosion and oxide dissolution in 316L stainless steel irradiated in situ in high temperature water, *J. Nucl. Mater.* 493 (2017) 207–218.
- [22] R.D. Hanbury, G.S. Was, Oxide growth and dissolution on 316L stainless steel during irradiation in high temperature water, *Corros. Sci.* 157 (2019) 305–311.
- [23] G.S. Was, J.T. Busby, T. Allen, E.A. Kenik, A. Jenison, S.M. Bruemmer, J. Gan, A. D. Edwards, P.M. Scott, P.L. Andreson, Emulation of neutron irradiation effects with protons: validation of principle, *J. Nucl. Mater.* 300 (2002) 198–216.
- [24] P. Deng, Q. Peng, E.H. Han, W. Ke, C. Sun, Z. Jiao, Effect of irradiation on corrosion of 304 nuclear grade stainless steel in simulated PWR primary water, *Corros. Sci.* 127 (2017) 91–100.
- [25] M. Boisson, L. Legras, E. Andrieu, L. Laffont, Role of irradiation and irradiation defects on the oxidation first stages of a 316L austenitic stainless steel, *Corros. Sci.* 161 (2019), 108194.
- [26] Z. Jiao, G. Was, Oxidation of a proton-irradiated 316 stainless steel in simulated BWR NWC environment, in: *Proceedings of the 15th International Conference on Environmental Degradation of Materials in Nuclear Power Systems-Water Reactors*, Colorado, USA, Colorado Springs, 2011.
- [27] A. Mazenc, S. Leclercq, A. Seyeux, A. Galtayries, P. Marcus, Influence of steam generator surface state on corrosion and oxide formation, in: *Proceedings of the Npc-Nuclear Plant Chemistry Conference*, Pairs, France, 2012.

- [28] R.P. Matthews, R.D. Knusten, J.E. Westraadt, T. Couvant, Intergranular oxidation of 316L stainless steel in the PWR primary water environment, *Corros. Sci.* 125 (2017) 175–183.
- [29] R.E. Stoller, M.B. Toloczko, G.S. Was, A.G. Certain, S. Dwaraknath, F.A. Garner, On the use of SRIM for computing radiation damage exposure, *Nucl. Instrum. Methods Phys. Res. Sect. B* 310 (2013) 75–80.
- [30] W. Kuang, X. Feng, D. Du, M. Song, M. Wang, G.S. Was, A high-resolution characterization of irradiation-assisted stress corrosion cracking of proton-irradiated 316L stainless steel in simulated pressurized water reactor primary water, *Corros. Sci.* 199 (2022), 110187.
- [31] W. Kuang, G. Was, The effect of grain boundary structure on the intergranular degradation behavior of solution annealed Alloy 690 in high temperature, hydrogenated water, *Acta Mater.* 182 (2019) 120–130.
- [32] S.E. Ziemniak, M. Hanson, Corrosion behavior of 304 stainless steel in high temperature, hydrogenated water, *Corros. Sci.* 44 (2002) 2209–2230.
- [33] W. Kuang, E.H. Han, X. Wu, J. Rao, Microstructural characteristics of the oxide scale formed on 304 stainless steel in oxygenated high temperature water, *Corros. Sci.* 52 (2010) 3654–3660.
- [34] W. Kuang, X. Wu, E.H. Han, The oxidation behaviour of 304 stainless steel in oxygenated high temperature water, *Corros. Sci.* 52 (2010) 4081–4087.
- [35] Z. Shen, J. Zhang, S. Wu, X. Luo, B.M. Jenkins, M.P. Moody, S. Lozano-Perez, X. Zeng, Microstructure understanding of high Cr-Ni austenitic steel corrosion in high-temperature steam, *Acta Mater.* 226 (2022), 117634.
- [36] D.J. Edwards, E.P. Simonen, S.M. Bruemmer, Evolution of fine-scale defects in stainless steels neutron-irradiated at 275°C, *J. Nucl. Mater.* 317 (2003) 13–31.
- [37] K.J. Stephenson, G.S. Was, Comparison of the microstructure, deformation and crack initiation behavior of austenitic stainless steel irradiated in-reactor or with protons, *J. Nucl. Mater.* 456 (2015) 85–98.
- [38] C. Pokor, Y. Brechet, P. Dubuisson, J.P. Massoud, A. Barbu, Irradiation damage in 304 and 316 stainless steels: experimental investigation and modeling. Part I: evolution of the microstructure, *J. Nucl. Mater.* 326 (2004) 19–29.
- [39] S.E. Ziemniak, M. Hanson, P.C. Sander, Electropolishing effects on corrosion behavior of 304 stainless steel in high temperature, hydrogenated water, *Corros. Sci.* 50 (2008) 2465–2477.
- [40] X. Lin, Q. Peng, J. Mei, E.H. Han, W. Ke, L. Qiao, Z. Jiao, Corrosion of phase and phase boundary in proton-irradiated 308L stainless steel weld metal in simulated PWR primary water, *Corros. Sci.* 165 (2020), 108401.
- [41] L. Dong, Q. Peng, E.H. Han, W. Ke, L. Wang, Stress corrosion cracking in the heat affected zone of a stainless steel 308L-316L weld joint in primary water, *Corros. Sci.* 107 (2016) 172–181.
- [42] X.X. Yu, M.A. Taylor, J.H. Perepezko, L.D. Marks, Competition between thermodynamics, kinetics and growth mode in the early-stage oxidation of an equimolar CoCrFeNi alloy, *Acta Mater.* 196 (2020) 651–659.
- [43] M. Kanzaki, Y. Masaki, T. Kudo, Effect of Cr and Ni on stress corrosion cracking susceptibility in Ni-Cr-Fe alloys under simulated pressurized water reactor primary conditions, *Corrosion* 71 (2015) 1027–1035.
- [44] X. Gong, M.P. Short, T. Auger, E. Charalampopoulou, K. Lambrinou, Environmental degradation of structural materials in liquid lead- and lead-bismuth eutectic-cooled reactors, *Prog. Mater. Sci.* 126 (2022), 100920.
- [45] L. Martinelli, F. Balbaud-Célérier, A. Terlain, S. Delpech, G. Santarini, J. Favregeon, G. Moulin, M. Tabarant, G. Picard, Oxidation mechanism of a Fe–9Cr–1Mo steel by liquid Pb–Bi eutectic alloy (Part I), *Corros. Sci.* 50 (2008) 2523–2536.
- [46] F. Rouillard, G. Moine, L. Martinelli, J.C. Ruiz, Corrosion of 9Cr Steel in CO₂ at intermediate temperature I: mechanism of void-induced duplex oxide formation, *Oxid. Met.* 77 (2012) 27–55.
- [47] W. Kuang, M. Song, G.S. Was, Insights into the stress corrosion cracking of solution annealed alloy 690 in simulated pressurized water reactor primary water under dynamic straining, *Acta Mater.* 151 (2018) 321–333.
- [48] M.J. Olszta, D.K. Schreiber, M.B. Toloczko, S.M. Bruemmer, Alloy 690 surface nanostructures during exposure to PWR primary water and potential influence on stress corrosion crack initiation, in: *Proceedings of the 16th International Conference on Environmental Degradation of Materials in Nuclear Power Systems-water Reactors*, Asheville, North Carolina, USA, 2013.
- [49] M.J. Olszta, D.K. Schreiber, L.E. Thomas, S.M. Bruemmer, Penetrative internal oxidation from alloy 690 surface and stress corrosion crack walls during exposure to PWR primary water, in: *Proceedings of the 15th International Conference on Environmental Degradation of Materials in Nuclear Power Systems-water Reactors*, Colorado, USA, Colorado Springs, 2011.
- [50] D.S. Morton, N. Lewis, M. Hanson, S. Rice, P. Sander, Nickel alloy primary water bulk surface and SCC film analytical characterization and SCC mechanism implications, in: *Proceedings of the 13th International Conference on Environmental Degradation of Materials in Nuclear Power Systems*, British Columbia, Whistler, 2007.
- [51] Q.C. Sherman, P.W. Voorhees, L.D. Marks, Thermodynamics of solute capture during the oxidation of multicomponent metals, *Acta Mater.* 181 (2019) 584–594.
- [52] I. Barin, *Thermochemical Data of Pure Substances*, Weinheim, 1989.
- [53] J. Gupta, J. Hure, B. Tanguy, L. Laffont, M.C. Lafont, E. Andrieu, Characterization of ion irradiation effects on the microstructure, hardness, deformation and crack initiation behavior of austenitic stainless steel: heavy ions vs protons, *J. Nucl. Mater.* 501 (2018) 45–58.
- [54] S. Wang, S. Zhang, J. Xie, X. Feng, M. Song, G.S. Was, W. Kuang, Clarifying the mitigation effect of proton irradiation on the intergranular oxidation of 316L stainless steel in high temperature water, *Acta Mater.* 241 (2022), 118408.
- [55] S. Ghosh, M.K. Kumar, V. Kain, High temperature oxidation behaviour of AISI 304L stainless steel – Effect of surface working operations, *Appl. Surf. Sci.* 264 (2013) 312–319.
- [56] H. Ming, Z. Zhang, J. Wang, R. Zhu, J. Ding, J. Wang, E.H. Han, W. Ke, Effect of surface state on the oxidation behavior of welded 308L in simulated nominal primary water of PWR, *Appl. Surf. Sci.* (2015).
- [57] S. Cissé, L. Laffont, B. Tanguy, M.C. Lafont, E. Andrieu, Effect of surface preparation on the corrosion of austenitic stainless steel 304L in high temperature steam and simulated PWR primary. water, *Corros. Sci.* 56 (2012) 209–216.
- [58] Z. Jiao, G.S. Was, Novel features of radiation-induced segregation and radiation-induced precipitation in austenitic stainless steels, *Acta Mater.* 59 (2011) 1220–1238.
- [59] L. Legras, M. Boisson, E. Fargeas, P. Cuvillier, R. Mercier, S. Miloudi, J. Tarabay, M. Roch, TEM investigations of the microstructure and oxides at the tip of intergranular cracks of a baffle former bolt irradiated up to 10 dpa, in: *Proceedings of the International Symposium Fontevraud IX*, Avignon, France, 2018.
- [60] L. Legras, A. Volgin, B. Radiguet, P. Pareige, C. Pokor, B. Décamps, T. Couvant, N. Huin, R. Soulas, Using Microscopy to help with the understanding of degradation mechanisms observed in materials of pressurized water reactors, *J. Mater. Sci. Eng. B* 7 (2017).
- [61] B. Langelier, S.Y. Persaud, R.C. Newman, G.A. Botton, An atom probe tomography study of internal oxidation processes in Alloy 600, *Acta Mater.* 109 (2016) 55–68.
- [62] M. Sennour, P. Laghoutaris, C. Guerre, R. Molins, Advanced TEM characterization of stress corrosion cracking of Alloy 600 in pressurized water reactor primary water environment, *J. Nucl. Mater.* 393 (2009) 254–266.
- [63] R.D. Hanbury, The Role of Displacement damage in Irradiation Affected Corrosion of 316L stainless Steel, University of Michigan, 2022. PhD thesis.
- [64] C. Xu, W. Gao, Pilling-Bedworth ratio for oxidation of alloys, *Mater. Res. Innov.* 3 (2000) 231–235.
- [65] M. Schütze, Mechanical properties of oxide scales, *Oxid. Met.* 44 (1995) 29–61.